The role of weak interactions in dynamic ejecta from binary neutron star mergers.

D. Martin[1,2], A. Perego[3,1,2,4,5], W. Kastaun[6,7], A. Arcones[1,2]

[1] Institut für Kernphysik, Technische Universität Darmstadt, Schlossgartenstraße 2, 64289 Darmstadt, Germany.

[2] GSI Helmholtzzentrum für Schwerionenforschung GmbH, Planckstraße 1, 64291 Darmstadt, Germany.

[3] Istituto Nazionale di Fisica Nucleare, Sezione di Milano-Bicocca, Gruppo Collegato di Parma, Parco Area delle Scienze 7/A 43124 Parma, Italy.

[4] Università degli Studi di Milano-Bicocca, Dipartimento di Fisica, Piazza della Scienza 3, 20126 Milano, Italy.

[5] Università degli Studi di Parma, Dipartimento di Matematica, Fisica e Scienze Informatiche, Parco Area delle Scienze 7/A 43124 Parma, Italy.

[6] Max Planck Institute for Gravitational Physics (Albert Einstein Institute), Callinstraße 38, 30167 Hannover, Germany.

[7] Leibniz Universität Hannover, Institute for Gravitational Physics, Callinstraße 38, 30167 Hannover, Germany.

E-mail: a.perego2@pr.infn.it

September 2017

Abstract. Weak reactions are critical for the neutron richness of the matter dynamically ejected after the merger of two neutron stars. The neutron richness, defined by the electron fraction ($Y_{\rm e}$), determines which heavy elements are produced by the r-process and thus directly impacts the kilonova light curve. In this work, we have performed a systematic and detailed post-processing study of the impact of weak reactions on the distribution of the electron fraction and of the entropy on the dynamic ejecta obtained from an equal mass neutron star binary merger simulated in full general relativity and with microscopic equation of state. Previous investigations indicated that shocks increase $Y_{\rm e}$, however our results show that shocks can also decrease $Y_{\rm e}$, depending on their thermodynamical conditions. Moreover, we have found that neutrino absorption are key and need to be considered in future simulations. We also demonstrated that the angular dependence of the neutrino luminosity and the spatial distribution of the ejecta can lead to significant difference in the electron fraction distribution. In addition to the detailed study of the $Y_{\rm e}$ evolution and its dependences, we have performed nucleosynthesis calculations. They clearly point to the necessity of improving the neutrino treatment in current simulations to be able to predict the contribution of neutron star mergers to the chemical history of the universe and to reliable calculate their kilonova light curves.

Keywords: Neutron stars, Weak interactions, r-process, Relativity and gravitation.

1. Introduction

The merger of two neutron stars is intrinsically a multi-messenger event. The energy that is released by these events produces a large variety of different transients, all of which are nowadays potentially detectable from the Earth (see, e.g., Rosswog (2015), Baiotti & Rezzolla (2017) and Fernández & Metzger (2016) for recent reviews). In the case of a sufficiently close event, we expect to observe gravitational waves from terrestrial detectors; electromagnetic radiation, ranging from gamma- and X-rays related with short gamma-ray bursts, to infrared emission associated with a kilonova (Metzger et al. 2010) (also called macronova, Kulkarni (2005)); and possibly neutrinos. Moreover, neutron star mergers play a critical role in the chemical evolution of the universe as they are most likely production site of half of the heavy elements via the rapid neutron capture process (r-process, Lattimer et al. 1977, Eichler et al. 1989, Bauswein et al. 2014). Indeed, the very neutron-rich isotopes that are formed and ejected in these events power the kilonova light curve as they decay to stability.

Our understanding of neutron star mergers is increasing very fast as computer power and observations improve. In current simulations, more microphysics has been included, namely high density equations of state (e.g., Hotokezaka et al. 2011, Bauswein et al. 2013, Read et al. 2013, Rezzolla & Takami 2016, Bernuzzi et al. 2016, Radice et al. 2017, Bovard et al. 2017) and neutrinos (e.g., Neilsen et al. 2014, Foucart et al. 2015, Sekiguchi et al. 2015, Radice et al. 2016). The transport of neutrinos produced in the hot and dense remnant is not full consistently included in current 3D, full general relativistic (GR) simulations. However, it has been shown that neutrinos and electron/positron captures are crucial to understand the evolution of the neutron richness (i.e., of the electron fraction, $Y_{\rm e}$) of the ejecta. This is the focus of our paper. Several questions concerning the evolution of the electron fraction in the dynamic ejecta still remain open and largely unexplored: What is the most relevant process responsible for the change in the electron fraction of the ejecta? What is the impact of shocks on the electron fraction? How robust is the r-process nucleosynthesis from binary neutron star (BNS) mergers under variations of the electron fraction?

Recent GR simulations, including microphysical equation of state (EOS) and neutrino treatment, indicate that the electron fraction of the dynamic ejecta can be significantly changed with respect to the initial cold weak equilibrium values (Wanajo et al. 2014, Sekiguchi et al. 2015, Foucart et al. 2015, Goriely et al. 2015, Radice et al. 2016, Bovard et al. 2017). Matter ejected by tidal interaction is expected to stay relatively cold. Therefore, in the absence of strong neutrino irradiation, its electron fraction should not change significantly (e.g., Korobkin et al. 2012). In contrast, matter ejected by shocks (occurring when the two neutron stars collide or after the remnant has formed) is heated up to significantly large temperatures. Under these conditions, electron-positron pairs are copiously produced and weak processes involving neutrinos can alter the initial electron fraction. In particular, positron captures on free neutrons can increase the electron fraction. Similarly, neutrino irradiation can enhance

the electron fraction through the absorption of electron neutrinos on the initially very neutron-rich ejecta.

In this paper, we consider trajectories of shock heated ejecta obtained from a GR hydrodynamical simulation (Kastaun et al. 2017). We include the impact of neutrino emission and absorption in a post-processing step, similar to Goriely et al. (2015), but including also consistently the consequences of weak reactions on the entropy evolution. Our approach allows to explore the role of individual weak reactions on the final distributions of electron fraction and entropy, and, in turn, on the detailed nucleosynthesis abundances. Our results indicate that the occurrence of a shock in the ejection process does *not necessary* lead to an increase of the electron fraction in neutron-rich matter, as found in previous works for other types of shock heated ejecta (e.g., Sekiguchi et al. 2015). If this is the case, neutrino absorption plays a major role in increasing $Y_{\rm e}$. We also study the dependence on the intensity of the neutrino irradiation and found a non-negligible effect on the nucleosynthesis. For the first time, we present the impact of neutrino emission anisotropies that can become very important and have strong consequences on the prediction of the final abundances and thus kilonova light curve.

The paper is structured as follows: In Sec. 2, we summarize the properties of the GR simulation that provides the dynamical evolution of the BNS merger, and we present the properties of the the ejecta obtained in that simulation and of the neutrino emission that we computed from the merger profiles. In Sec. 3, we introduce the post-processing treatment for the weak reactions to evolve the electron fraction and entropy of each tracer. Sec. 4 is devoted to the presentation and discussion of our results in terms of distributions of the properties of the ejecta and of abundances of the nucleosynthesis yields. Finally, in Sec. 5, we draw our conclusions.

2. Binary NS merger simulation

2.1. Setup and numerical evolution

The ejected matter data studied in this work are extracted from one of the numerical simulations described in Kastaun et al. (2017). The `SHT_UU` model consists of two NSs with gravitational mass of $1.4\,M_\odot$ each, and employs the EOS by Shen, Horowitz, Teige (SHT, Shen et al. 2010, Shen et al. 2011). The initial NS spins are aligned with the orbital angular momentum, with dimensionless spin $J/M^2 \approx 0.125$. We note that the other spin configurations studied in Kastaun et al. (2017) did not yield a significant amount of ejecta. For the SHT EOS, the maximum possible baryonic (gravitational) mass of a non-rotating NS (at zero temperature in β-equilibrium) is $3.33\ M_\odot$ ($2.77\ M_\odot$), which is unusually large. Since the total baryonic mass of the system is below this critical value, the merger remnant is a stable NS (which we regard as an astrophysical corner case).

The numerical evolution was carried out in general relativity and the matter was

treated as a perfect fluid. Pressure, internal energy, and specific entropy were computed from density, temperature, and electron fraction using a three-dimensional interpolation table of the SHT EOS, as described in Galeazzi et al. (2013). We did not include magnetic fields (which might drive further matter outflows in addition to dynamical ejecta, Siegel et al. (2014)). The code made use of moving box mesh refinement, with a finest resolution of 295 m, and the outer boundary is located at 945 km. The numerical methods and code set-up are described in detail in Kastaun et al. (2017). Neutrino radiation was not taken into account in the simulation itself, and the electron fraction was passively advected with the fluid. In this study, we account for the neutrino physics in a post-processing step, which will be described in Sec. 2.3, neglecting any impact on the fluid dynamics in the remnant.

One technical detail relevant for this work is the usage of an artificial atmosphere, which is a standard method where a minimum mass density is enforced throughout the computational domain, and the velocity is set to zero inside the artificial atmosphere. This is required because the hydrodynamic equations degenerate in vacuum and also because our tabulated EOS does not extend to arbitrary low values. Due to the latter, we used a relatively dense atmosphere of 6×10^7 g cm^{-3} (with temperature 0.06 MeV and electron fraction 0.4). Although such an atmosphere only weakly affects the dynamics of the inspiral, merger remnant, and disk, it has a strong impact on the low-density ejecta (see the discussion in Endrizzi et al. 2016, Kastaun & Galeazzi 2015*a*). We stress that, since the goal of this work is to study the impact of weak reactions on the properties of the ejecta, the potential effect of the artificial atmosphere on the total amount of ejected material and (more importantly) the escape velocity, has no relevance for us. That said, we do make use of a method developed to correct for the drag, which will be described in Appendix B.

2.2. Ejecta and tracers

Extracting the trajectories of ejected matter from a numerical simulation is a nontrivial task that requires various approximations. In the following, we describe the main difficulties and the solutions used for this work. The first challenge is that numerical simulations can only be run on short time scales, necessitating a criterion to judge if a given fluid element will reach infinity eventually. For this, we use the standard approach of assuming geodesic motion, approximating the spacetime as stationary. This results in the condition $u_t < -1$, where u is the fluid 4-velocity (e.g., Kastaun & Galeazzi 2015*b*). Although physically we do not expect significant deviations from Keplerian motion once the ejected matter is expelled from the vicinity of merger remnant and disk, the artificial atmosphere (see previous section) causes an unphysical drag force. In our case, the impact is quite strong because of the low ejecta mass (and hence density) and the high atmosphere density. Almost all matter that was unbound at some point becomes bound again at large radii. We attribute this to the spurious drag force based on an animation (available in the supplemental material of Kastaun et al. (2017)) showing

how regions of unbound matter run into the artificial atmosphere and slowly dissolve. In Kastaun et al. (2017), we measured the flux of unbound matter through spherical surfaces of increasing radius and used the maximum as an estimate for the amount of ejected matter. For this work however, we require the trajectories of ejected matter up to radii much larger than the simulation domain. Therefore, we extrapolated trajectories assuming Keplerian motion when the drag force becomes relevant. To determine this correction, we constructed a simple model for the atmospheric drag, which we also use to validate that the artificial atmosphere is the reason for the decrease of unbound mass at large radius. The details of this model are presented in Appendix B.

The next challenge is to extract fluid trajectories from the numerical simulation, which uses a numerical grid to describe the fluid (in contrast to smoothed particle hydrodynamics codes, for which trajectories are an integral part of the evolution). One approach would be to follow tracers during the evolution (Bovard & Rezzolla 2017). A difficulty with that method is the placement of the initial tracer positions. Since only a small fraction of the fluid mass ends up as ejected matter, a large fraction of tracers will be wasted. Achieving a good coverage of ejected matter becomes computationally challenging. To overcome this limitation, we extracted the fluid trajectories in a post-processing step from 3D data saved during the evolution. One shortcoming of this procedure is that the data need to be stored with sufficiently high resolution in both space and time to maintain accuracy in the integration. However, it has the advantage that we can identify unbound material at a suitable time and then trace its movement both forward and backward in time. In our case, most matter became unbound during a few ms. This allowed us to simplify the code and start the time integration of all tracers at the same seed time, where the amount of unbound matter becomes maximal. The seed positions are taken from a regular grid, and we assign the mass proportionally to the local density. Only grid points with $u_t < -1+\delta$ are used as seed positions. We lower the threshold for the unbound matter criterion by some suitable $\delta > 0$ to make up for the fact that some matter becomes unbound later or re-bound earlier. After computing the trajectories we remove the ones that never became unbound. Starting from the seed positions, we integrate both forward and backward in time, using a second order scheme and cylindrical coordinates. A further complication of the artificial atmosphere is that the least dense parts of the ejecta fall below the cutoff density at some point, and become part of the non-moving atmosphere. We only keep trajectories that can be traced to the end. Finally, we combine neighboring trajectories in order to limit the number of trajectories to $\approx$1000, since the nuclear network calculations using the trajectories are more expensive than the extraction. We have tested that this procedure has practically no impact on our analysis.

We find that the ejecta for the model at hand are neither tidally ejected nor part of a breakout shock formed when the stars merge. Instead, the ejecta originate from the inner part of the disk. Around 2 ms after merger, one of the remnant oscillations sends a wave into the disk, which liberates the marginally bound matter. The ejecta form two concentric rings above and below the orbital plane, which expand radially

(and also in z-direction). We note that it does not require any violent movement of the remnant to eject matter, because the density scales are very different. In our example, it appears that a wave steepens into a shock. At least, we found a steep increase of specific entropy (from a few to $\sim 7\,k_\mathrm{B}\,\mathrm{baryon}^{-1}$) at the same time the ring starts accelerating outwards. The average ejecta temperature (entropy) is increased from about 10 GK to about 30 GK by the shock heating, and then cools down adiabatically while the density is decreasing. It is important to mention that most material is still classified as bound when the temperature has already dropped below NSE conditions. Since the temperature enters into the initial conditions for nucleosynthesis calculations, it is necessary to know the thermal history of unbound matter. Using the conditions found at the time where matter becomes unbound is only sufficient for tidally ejected (i.e., cold) matter. Mass-weighted average temperature and radius for the (Kepler-extrapolated) tracers are shown in Figure 1. The correlation between acceleration and temperature increase is clearly visible. Note that near the end the temperature slightly increases again. We assume that in addition to the drag, the interaction with the artificial atmosphere also causes heating. However, before performing our analysis we correct this artificial increase, by assuming constant entropy outside a fiducial radius of 200 km. Finally, as an independent validation of the correct tracing of fluid elements, we compute the radial extent of unbound matter at each time directly from data on the numerical grid. For this, we collect at regular time intervals the unbound mass in histograms with bins corresponding to the radial coordinate. The resulting unbound regions are also shown in Figure 1. The bulk of the trajectories are clearly inside this region, although, as described above, some trajectories also become bound again. The Figure also shows the impact of the drag correction, which will be described in Appendix B.

2.3. Neutrino properties

Numerical simulations of BNS mergers, including neutrino emission, show characteristic trends in the evolution of the neutrino luminosities, L_ν, and mean energies, $\langle E_\nu \rangle$ (Ruffert et al. 1997, Rosswog & Liebendörfer 2003, Neilsen et al. 2014, Foucart et al. 2015, Sekiguchi et al. 2015, Radice et al. 2016). While the emission of radiation is negligible during the cold inspiral phase, as soon as the two NSs touch ($t = t_\mathrm{m}$) and the temperature in the remnant increases, neutrino luminosities are boosted and reach their peak values (a few $10^{53}\,\mathrm{erg\,s^{-1}}$) within a few ms ($t = t_\mathrm{peak}$). Additionally, the neutrino mean energies rise, as a consequence of the temperature growth. After a few oscillations (lasting typically no more than a few ms, and related with the motion of the merging cores and the formation of the disk), both the luminosities and the mean energies settle to almost stationary values. On a longer time scale, the luminosities slowly decrease as a result of the remnant and disk cooling, and of the reduction of the accretion rate inside the disk. To mimic this behavior, we model the neutrino luminosities according

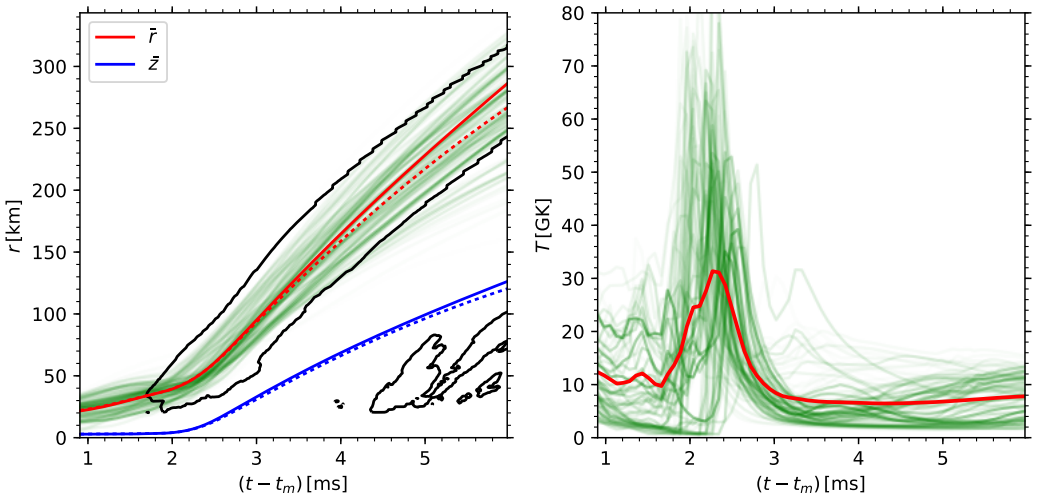

Figure 1. Properties of the ejected tracers versus time after merger, $t_{\rm m}$. Left: spherical radial coordinate and z coordinate. The solid blue and red lines represent the mass-weighted average of the tracer positions after correcting for the atmospheric drag, the dotted lines the same without the correction. The transparent lines show individual tracer trajectories (opacity proportional to mass). The contour line shows regions with unbound material (no drag correction) obtained directly from the numerical grid by summing unbound mass into histograms over radial bins at regular times. Right: Matter temperature. Thick black lines represent averages over the whole tracer sample (weighting each individual trajectory by its mass). The transparent lines represent individual trajectories.

to the following analytic prescription:

$$L_\nu(t) = \begin{cases} 0 & \text{for} \quad t \le t_{\rm m}, \\ L_{\nu,\rm peak} \left(\frac{t-t_{\rm m}}{t_{\rm peak}-t_{\rm m}} \right) & \text{for} \quad t_{\rm m} < t \le t_{\rm peak}, \\ L_{\nu,\rm peak} \, \exp\left(-\frac{t-t_{\rm m}}{\Delta t_{\rm cool}} \right) & \text{for} \quad t > t_{\rm peak}, \end{cases} \tag{1}$$

where we have included the growth of the luminosities between $t_{\rm m}$ and $t_{\rm peak}$, and the subsequent decrease, but have neglected the transient oscillations. In the previous equation, t is the time with respect to the beginning of the simulation. We consider a typical cooling time scale $\Delta t_{\rm cool} \sim 500\,$ms, comparable with the disk life time and with the diffusion time scale from the central MNS (e.g., Dessart et al. 2009, Perego et al. 2014). We note that its precise value is of small importance, since $\Delta t_{\rm cool}$ is much larger than $t_{\rm peak}$ and the tracer expansion time scale. The parameters $t_{\rm m}$ and $t_{\rm peak}$ are determined through a careful inspection of the merger simulation. In particular, $t_{\rm m} = 12.5\,$ms is the time where the total entropy starts to increase due to the NS collision and $t_{\rm peak} = 17.5\,$ms when it reaches an almost stationary value. Similarly, for the neutrino mean energies we assume an initial linear increase, followed by an almost

stationary phase:

$$\langle E_\nu \rangle(t) = \begin{cases} \langle E_{\nu,\min} \rangle & \text{for} \quad t \leq t_{\rm m}, \\ \langle E_{\nu,\min} \rangle + \langle \Delta E_\nu \rangle \left(\frac{t - t_{\rm m}}{t_{\rm peak} - t_{\rm m}} \right) & \text{for} \quad t_{\rm m} < t \leq t_{\rm peak}, \\ \langle E_{\nu,\max} \rangle & \text{for} \quad t > t_{\rm peak}\,, \end{cases} \tag{2}$$

where $\langle \Delta E_\nu \rangle \equiv (\langle E_{\nu,\max} \rangle - \langle E_{\nu,\min} \rangle)$.

Luminosities and mean energies are used to compute local neutrino fluxes $\mathcal{F}_\nu$. Far from the neutrino emission region, we expect purely radial fluxes, axisymmetric around the rotational axis of the remnant. We further assume a quadratic dependence on $\cos\theta$:

$$\mathcal{F}_\nu(R, \theta, t) = \frac{3\,(1 + \alpha \cos^2\theta)}{3 + \alpha} \frac{L_\nu(t)}{4\pi R^2 \, \langle E_\nu \rangle(t)}\,, \tag{3}$$

where θ is the polar angle from the rotational axis and R the distance from the remnant center. For $\alpha = 0$, we recover the isotropic case. For $\alpha = 2$, we mimic the modulation of the flux due to the presence of the optically thick disk. In fact, along the equator ($\theta = \pi/2$) $\mathcal{F}_\nu$ has its minimum, while along the poles ($\theta = 0$) it reaches its maximum. Numerical results of the neutrino emission from merger remnants point to $\mathcal{F}_\nu(R, \theta = 0, t)/\mathcal{F}_\nu(R, \theta = \pi/2, t) \approx 3$ (Dessart et al. 2009, Perego et al. 2014) and are well described by $\alpha \approx 2$.

The original simulation does not model the neutrino emission. Thus, we compute the neutrino properties associated with the merger remnant in a post-processing step. We map the outcome of a general relativistic binary merger simulation‡ into the `FISH+ASL` code (Käppeli et al. 2011, Perego et al. 2016). The latter has been extensively employed to study the evolution of binary merger remnants and their neutrino emission (Perego et al. 2014, Martin et al. 2015). For the mapping, we choose a time step corresponding to $\sim$ 15 ms after the first touch $t_{\rm m}$. At this time, the remnant is characterized by an approximately axisymmetric massive neutron star, surrounded by a thick accretion disk. Since `FISH` is a Newtonian Cartesian hydrodynamical code, a further approximation becomes necessary because the geometry of the spacetime in a NS is strongly non-Euclidean. We chose a mapping as follows: first, we approximate the spacetime as spherically symmetric and extract the corresponding metric coefficients from the available 1D data along the x axis. Then the volume element after transforming back to Cartesian coordinates becomes unity. This way, volume integrals in the Newtonian geometry (in particular the total mass) yield approximately the correct GR result, while distances are distorted.

In the original simulation, the initial cold ($T = 0$) beta-equilibrium electron fraction is simply advected. However, weak reactions at high temperatures and densities are expected to change the relative amount of neutrons and protons, as a results of an asymmetric behavior of electron neutrinos and antineutrinos. In particular, $L_{\bar{\nu}_{\rm e}} > L_{\nu_{\rm e}}$ (Eichler et al. 1989, Ruffert et al. 1997, Rosswog & Liebendörfer 2003) and the formation

‡ Since the 3D distribution of Y_e was not saved for the simulation presented in the previous section, we computed the neutrino emission from the output of an almost identical simulation, in which the initial NS are irrotational.

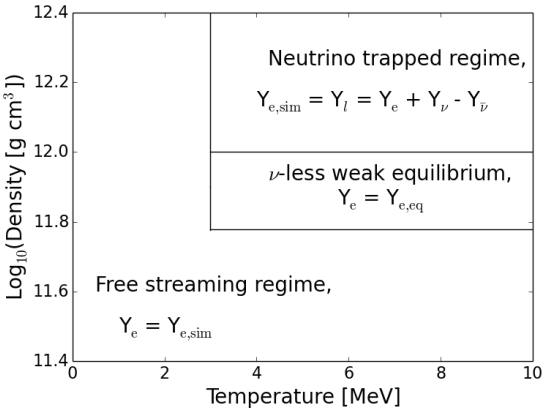

Figure 2. Summary of the different regimes adopted to set the initial Y_e in the calculation of the neutrino luminosities and mean energies. The electron fraction obtained in the original simulation is possibly changed according to the thermodynamical conditions inside the remnant. After the initialization, Y_e evolves according to the leakage prescription. See the text for more details.

of an excess of $\bar{\nu}_\mathrm{e}$ deep inside the hot remnant (Foucart et al. 2015) increase the proton and electron abundances. To take these effects into account, we distinguish between different regimes (also summarized in Figure 2) to initialize Y_e:

- The neutrino trapped regime; due to both high density $\rho > \rho_\mathrm{eq} = 10^{12}\,\mathrm{g\,cm^{-3}}$ and temperature $T \gtrsim 3\,\mathrm{MeV}$, neutrinos diffuse on a time scale longer than the dynamical time scale. Thus, neutrinos are trapped and the electron fraction obtained from the simulation is assumed to be equal to the total lepton fraction, $(Y_\mathrm{e})_\mathrm{sim} = Y_\mathrm{l} = Y_\mathrm{e} + Y_{\nu_\mathrm{e}} - Y_{\bar{\nu}_\mathrm{e}}$. The actual values for Y_e, Y_{ν_e}, and $Y_{\bar{\nu}_\mathrm{e}}$ are computed assuming weak equilibrium.
- The hot, neutrinoless beta-equilibrium regime; for $\rho_\mathrm{free} = 5 \cdot 10^{11}\,\mathrm{g\,cm^{-3}} < \rho < \rho_\mathrm{eq} = 10^{12}\,\mathrm{g\,cm^{-3}}$, and $T \gtrsim 3\,\mathrm{MeV}$, neutrino reactions are still fast enough to change Y_e on a very short time scale ($\lesssim 1\,\mathrm{ms}$), but neutrino diffusion happens on the same time scale. Under these conditions, we initialize Y_e assuming hot, neutrinoless beta-equilibrium.
- The neutrino free-streaming regime. For $\rho < \rho_\mathrm{free}$ or low matter temperature, the locally produced neutrinos can stream away. For this region, we initially assume that $Y_\mathrm{e} = (Y_\mathrm{e})_\mathrm{sim}$.

Due to the differences between the original GR simulation and the Newtonian character of the `FISH` code, we do not dynamically evolve the remnant, but we consider its distribution of matter as a stationary background, and we evolve only the electron fraction and the temperature due to the neutrino emission. In Figure 3, we present the temporal evolution of the electron neutrino and antineutrino luminosities (left panel) and mean energies (right panel), obtained once the simulation has been started. We stress that these temporal profiles do not represent the true physical evolution of the neutrino

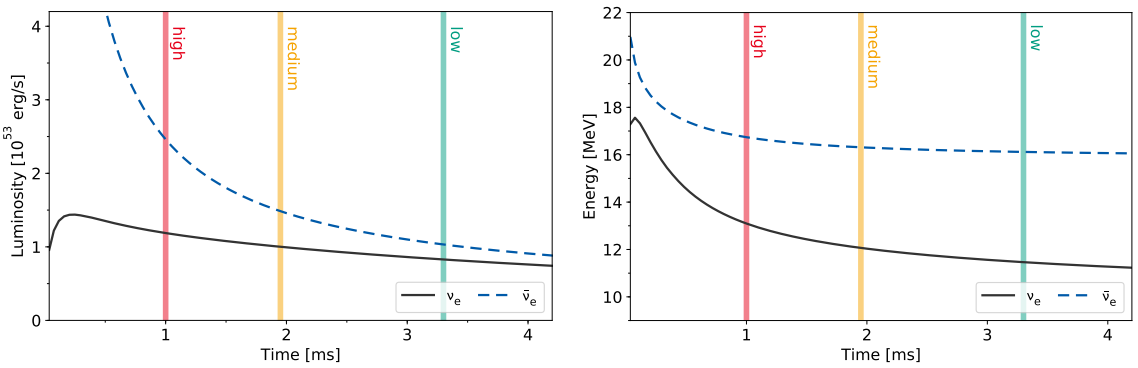

Figure 3. Temporal profiles of the neutrino luminosities (left) and mean energies (right) obtained by post-processing with the `FISH+ASL` code a snapshot of three dimensional results of the the GR hydrodynamics simulation described in Sec. 2, once the disk has formed. Neutrino cooling feedback is included only in the temperature and electron fraction evolutions, while matter is considered as a stationary background. Thus, these temporal profiles should be intended as a sequence of possible weak equilibrium configurations (after an initial transient phase), rather than a temporal evolution. Vertical bands represent three possible configuration, chosen to bracket uncertainties in the determination of the neutrino properties immediately after the merger.

quantities, since these can be obtained only by a consistent radiation-hydrodynamical model. They rather represent a fast approach to (T, Y_e) quasi-equilibrium configurations from an initial non-equilibrium state. In particular, during the first ms, the excess of neutrons in the free streaming regime produces a large $L_{\bar{\nu}_e}$ (several $10^{53}\,\mathrm{erg\,s^{-1}}$), which rapidly changes the electron fraction for $\rho \lesssim \rho_{\rm free}$. This determines a sudden decrease of $L_{\bar{\nu}_e}$. After $\sim 1\,\mathrm{ms}$, the electron fraction in the remnant has settled to a steady configuration and the luminosities decrease smoothly, due to the remnant and disk cooling. We use the obtained temporal profiles of the luminosities and mean energies to select three different sets of values, (referred to as high, medium and low), to span the uncertainties in the determination of the neutrino properties, as well as the large range of values obtained in different models. For $\langle E_{\nu,\rm min}\rangle$, we take 8 MeV for both ν_e and $\bar{\nu}_e$. In Tab. 1, we summarize all the parameters later used in Eqs. (1) and (2). We have also tested that the behavior of the luminosities after 1 ms is only weakly dependent from the detailed choice of the boundary values (e.g., $\rho_{\rm eq}$ and $\rho_{\rm free}$) in the Y_e initialization.

3. Coupling weak interactions with tracer evolution

We post-process the tracers obtained from the simulation to include the impact of neutrino emission and absorption on the evolution of the electron fraction and of the entropy.

If $t_{\rm init}$ and t_o denote the starting and the ending point of each tracer, we solve the

Table 1. Parameters for the maximum neutrino and antineutrino luminosities and energies. In the beginning, we assume vanishing luminosities $L_{\nu_e,\min} = L_{\bar{\nu}_e,\min} = 0$ and constant energies $\langle E_{\nu_e,\min}\rangle = \langle E_{\bar{\nu}_e,\min}\rangle = 8\,\mathrm{MeV}$.

Name	$L_{\nu_e,\max}$ $[10^{53}\,\mathrm{erg\,s^{-1}}]$	$L_{\bar{\nu}_e,\max}$ $[10^{53}\,\mathrm{erg\,s^{-1}}]$	$\langle E_{\nu_e,\max}\rangle$ [MeV]	$\langle E_{\bar{\nu}_e,\max}\rangle$ [MeV]
capture	0.0	0.0	0.0	0.0
low	0.86	1.0	11.5	16.2
medium	1.0	1.5	12.0	16.3
high	1.2	2.4	13.0	16.7

following system of coupled ordinary differential equations for $t_{\mathrm{init}} < t \leq t_{\mathrm{o}}$:

$$\frac{\mathrm{d}\rho}{\mathrm{d}t} = \left(\frac{\mathrm{d}\rho}{\mathrm{d}t}\right)_{\mathrm{hydro}}(t)\,, \tag{4}$$

$$\frac{\mathrm{d}\mathbf{x}}{\mathrm{d}t} = \left(\frac{\mathrm{d}\mathbf{x}}{\mathrm{d}t}\right)_{\mathrm{hydro}}(t)\,, \tag{5}$$

$$\frac{\mathrm{d}Y_{\mathrm{e}}}{\mathrm{d}t} = \left(\frac{\mathrm{d}Y_{\mathrm{e}}}{\mathrm{d}t}\right)_{\nu}(t)\,, \tag{6}$$

$$\frac{\mathrm{d}s}{\mathrm{d}t} = \left(\frac{\mathrm{d}s}{\mathrm{d}t}\right)_{\mathrm{hydro}}(t) + \left(\frac{\mathrm{d}s}{\mathrm{d}t}\right)_{\nu}(t)\,. \tag{7}$$

On the lhs, ρ is the matter density, $\mathbf{x}$ the particle position, Y_{e} the electron fraction and s the matter entropy per baryon. On the rhs, time derivatives labeled by "hydro" refer to the evolution obtained inside the simulations, while the ones label by "ν" denote the variation due to the interaction with neutrinos. At $t = t_{\mathrm{o}}$, temperatures are usually larger than 10 GK. We extend the evolution also to $t > t_{\mathrm{o}}$ up to the point $t = t_{\mathrm{end}}$ when the temperature reaches 3 GK, assuming homologous expansion without shocks ($(\mathrm{d}s/\mathrm{d}t)_{\mathrm{hydro}} = 0$) and constant velocity:

$$\frac{\mathrm{d}\rho}{\mathrm{d}t} = -3\frac{\rho_o}{t}\left(\frac{t_{\mathrm{o}}}{t}\right)^3\,, \tag{8}$$

$$\frac{\mathrm{d}\mathbf{x}}{\mathrm{d}t} = \left(\frac{\mathrm{d}\mathbf{x}}{\mathrm{d}t}\right)_{\mathrm{hydro}}(t_{\mathrm{o}})\,, \tag{9}$$

$$\frac{\mathrm{d}Y_{\mathrm{e}}}{\mathrm{d}t} = \left(\frac{\mathrm{d}Y_{\mathrm{e}}}{\mathrm{d}t}\right)_{\nu}(t)\,, \tag{10}$$

$$\frac{\mathrm{d}s}{\mathrm{d}t} = \left(\frac{\mathrm{d}s}{\mathrm{d}t}\right)_{\nu}(t)\,. \tag{11}$$

We note that this expansion is identical to the one used inside the network to evolve the tracers for much longer time. This ensures a smooth transition between the tracer post-processing and the nuclear network calculations. We have chosen 3 GK as a limiting temperature because for all our tracers it is below the temperature where the network

starts to compute detailed abundances out of NSE. We have verified that our results are independent from this choice.

To compute the variations due to neutrinos, $\left(\mathrm{d}Y_\mathrm{e}/\mathrm{d}t\right)_\nu$ and $\left(\mathrm{d}s/\mathrm{d}t\right)_\nu$, we consider a subset of reactions comprising the most relevant charged-current reactions between neutrinos and matter, namely the capture of electron, positron, electron neutrinos and antineutrinos on free nucleons:

$$\mathrm{p} + \mathrm{e}^- \rightarrow \mathrm{n} + \nu_\mathrm{e}\,, \tag{12}$$

$$\mathrm{n} + \mathrm{e}^+ \rightarrow \mathrm{p} + \bar{\nu}_\mathrm{e}\,, \tag{13}$$

$$\mathrm{n} + \nu_\mathrm{e} \rightarrow \mathrm{p} + \mathrm{e}^-\,, \tag{14}$$

$$\mathrm{p} + \bar{\nu}_\mathrm{e} \rightarrow \mathrm{n} + \mathrm{e}^+\,. \tag{15}$$

For each capture reaction, we compute the associated reaction rates λ_x for species $x = \mathrm{e}^-, \mathrm{e}^+, \nu_\mathrm{e}, \bar{\nu}_\mathrm{e}$ and we distinguish between particle (λ^0_x) and energy (λ^1_x) rates. The variation for the electron fraction is

$$\left(\frac{\mathrm{d}Y_\mathrm{e}}{\mathrm{d}t}\right)_\nu = \left(\lambda^0_{\nu_\mathrm{e}} + \lambda^0_{\mathrm{e}^+}\right) Y_\mathrm{n} - \left(\lambda^0_{\bar{\nu}_\mathrm{e}} + \lambda^0_{\mathrm{e}^-}\right) Y_\mathrm{p} \equiv \lambda^0_+ Y_\mathrm{n} - \lambda^0_- Y_\mathrm{p}\,, \tag{16}$$

where Y_n and Y_p are the abundances of free neutrons and protons, respectively.

For the entropy variation, from the first principle of thermodynamics we obtain

$$\left(\frac{\mathrm{d}s}{\mathrm{d}t}\right)_\nu = \frac{1}{T}\left[\left(\frac{\mathrm{d}Q}{\mathrm{d}t}\right)_\nu - \left(\mu_\mathrm{e} - \mu_\mathrm{n} + \mu_\mathrm{p}\right)\left(\frac{\mathrm{d}Y_\mathrm{e}}{\mathrm{d}t}\right)_\nu\right]\,, \tag{17}$$

where $\left(\mathrm{d}Q/\mathrm{d}t\right)_\nu$ is the heat variation due to the emission and absorption of neutrinos:

$$\left(\frac{\mathrm{d}Q}{\mathrm{d}t}\right)_\nu = \left(\lambda^1_{\nu_\mathrm{e}} - \lambda^1_{\mathrm{e}^+}\right) Y_\mathrm{n} + \left(\lambda^1_{\bar{\nu}_\mathrm{e}} - \lambda^1_{\mathrm{e}^-}\right) Y_\mathrm{p}\,, \tag{18}$$

and μ_e, μ_p and μ_n are the chemical potentials of electrons, protons and neutrons, respectively. The particle and energy capture rates are computed according to (Bruenn 1985), including the corrections due to the electron mass, $\mathcal{M}$, and to the weak magnetism $\mathcal{R}_{\nu_\mathrm{e},\bar{\nu}_\mathrm{e}}$:

$$\begin{aligned}\lambda^k_{e^-} = {} & \frac{4\pi\sigma_0 c}{(2\pi\hbar c)^3}\int_0^\infty \left(\frac{E+\Delta}{m_\mathrm{e}}\right)^2 \mathcal{M}(E+\Delta)\,\mathcal{R}_{\nu_\mathrm{e}}(E)\, f_{\mathrm{e}^-}(E+\Delta) \\ & \times E^{2+k}\,\mathrm{d}E\,,\end{aligned} \tag{19}$$

$$\begin{aligned}\lambda^k_{e^+} = {} & \frac{4\pi\sigma_0 c}{(2\pi\hbar c)^3}\int_{\Delta+m_\mathrm{e}}^\infty \left(\frac{E-\Delta}{m_\mathrm{e}}\right)^2 \mathcal{M}(E-\Delta)\,\mathcal{R}_{\bar{\nu}_\mathrm{e}}(E)\, f_{\mathrm{e}^+}(E-\Delta) \\ & \times E^{2+k}\,\mathrm{d}E\,,\end{aligned} \tag{20}$$

$$\begin{aligned}\lambda^k_{\nu_\mathrm{e}} = {} & \frac{\mathcal{G}_{\nu_\mathrm{e}}\sigma_0 c}{(2\pi\hbar c)^3}\int_0^\infty \left(\frac{E+\Delta}{m_\mathrm{e}}\right)^2 \mathcal{M}(E+\Delta)\,\mathcal{R}_{\nu_\mathrm{e}}(E)\,\left[1 - f_{\mathrm{e}^-}(E+\Delta)\right] \\ & \times f_{\nu_\mathrm{e}}(E)\, E^{2+k}\,\mathrm{d}E\,,\end{aligned} \tag{21}$$

$$\begin{aligned}\lambda^k_{\bar{\nu}_\mathrm{e}} = {} & \frac{\mathcal{G}_{\bar{\nu}_\mathrm{e}}\sigma_0 c}{(2\pi\hbar c)^3}\int_{\Delta+m_\mathrm{e}}^\infty \left(\frac{E-\Delta}{m_\mathrm{e}}\right)^2 \mathcal{M}(E-\Delta)\,\mathcal{R}_{\bar{\nu}_\mathrm{e}}(E)\,\left[1 - f_{\mathrm{e}^+}(E-\Delta)\right] \\ & \times f_{\bar{\nu}_\mathrm{e}}(E)\, E^{2+k}\,\mathrm{d}E\,,\end{aligned} \tag{22}$$

where c is the speed of light, m_e the electron mass, $\Delta = 1.2935\,\mathrm{MeV}$ the mass difference between neutron and proton, and $\sigma_0 = 4(m_\mathrm{e}c^2)^2 G_F^2 (c_v^2 + 3c_a^2)/\pi\hbar^4 \approx 2.43 \times 10^{-44}\,\mathrm{cm}^2$ with G_F the Fermi constant, $\hbar$ the reduced Planck constant, $c_v = 1$ and $c_a = g_a \approx 1.23$. The distribution functions of electrons and positrons, $f_{\mathrm{e}^\mp}$, are assumed to obey Fermi-Dirac distributions with non-vanishing chemical potentials. The electron mass correction term is $\mathcal{M}(x) = \left(1 - (m_\mathrm{e}/x)^2\right)^{1/2}$, while the weak magnetism factors, $\mathcal{R}_{\nu_\mathrm{e},\bar{\nu}_\mathrm{e}}$, are implemented according to Horowitz (2002). Their detailed expressions are provided in Appendix A. Free-streaming neutrinos and antineutrinos are assumed to be described by a distribution function with a Fermi-Dirac energy spectrum of temperature T_ν and zero degeneracy, and with an angular dependence g_ν,

$$f_\nu(E,\Omega) = g_\nu(\Omega)\,\frac{1}{1+\exp\left(\frac{E}{k_\mathrm{B}T_\nu}\right)}\,, \tag{23}$$

such that

$$\mathcal{G}_\nu = \int_\Omega g_\nu(\Omega)\mathrm{d}\Omega\,. \tag{24}$$

The value of $\mathcal{G}_\nu$ can be expressed in terms of the local neutrino density and, ultimately, of the neutrino luminosity and mean energy:

$$\mathcal{G}_\nu = \frac{L_\nu}{4\pi r^2 \langle E_\nu\rangle c}\frac{(2\pi\hbar c)^3}{(k_\mathrm{B}T_\nu)^3 F_2(0)}\,, \tag{25}$$

where $F_k(\eta) \equiv \int_0^\infty x^k/[1+\exp(x-\eta)]\,\mathrm{d}x$ is the Fermi integral of order k evaluated at η. In the rates calculations, we have included Pauli blocking factors for electrons and positrons in the final states, while we have neglected neutrino blocking factors in free streaming conditions.

Hot and dense matter in NSE is described by a nuclear equation of state in tabular form (Hempel et al. 2012). For consistency with the underlying simulation, we choose the NL3 parameterization for the nucleon interaction. However, since our initial densities are usually below $10^{13}\,\mathrm{g\,cm^{-3}}$, we do not expect our choice to have a significant impact on the results.

For each trajectory, we assume as initial conditions for the matter density, entropy, and velocity the tracer properties at $t = t_\mathrm{init}$, such that $\rho(t_\mathrm{init}) = 10^{12}\,\mathrm{g\,cm^{-3}} \equiv \rho_\mathrm{eq}$. We consider this value for ρ as the transition between the diffusive and the free-streaming regime for neutrinos (see Sec. 3). A precise initialization of the electron fraction would require a detailed evolution of Y_e inside the merger simulation in neutrino diffusive conditions. Since this is not available, we consider two opposite cases:

- Case A, in which weak equilibrium is assumed down to ρ_eq. This corresponds to the case where neutrino reactions are fast enough (compared to the expansion time scale) to drive Y_e toward the equilibrium value associated with the corresponding density and temperature, $Y_\mathrm{e,eq}$. If the tracer starts at a density below ρ_eq§, then $Y_\mathrm{e} = 0.044$ is assumed (this value corresponds to mass-weighted average Y_e of ejecta passing through a spherical surface of radius 111 km in the original simulation).

§ This condition is fulfilled for $\sim 25\%$ of the tracers.

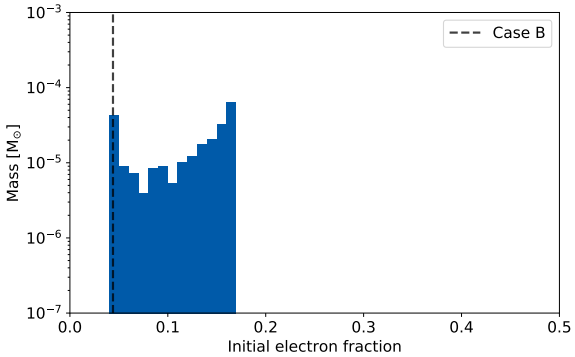

Figure 4. Mass distribution of the electron fraction of the ejecta at the beginning of the post-processing calculations for case A, (i.e., assuming weak equilibrium up to $t_{\rm init}$ when matter density drops below $\rho_{\rm eq}$). Case B corresponds to the vertical line at $Y_{\rm e} = 0.044$.

- Case B, where $Y_{\rm e} = 0.044$ is assumed for every tracer at $t = t_{\rm init}$. This corresponds to the case where all neutrino reactions are very slow for $\rho > \rho_{\rm eq}$, compared to the expansion time scale, and the electron fraction remains practically unchanged.

For most of the tracers, temperatures are usually smaller than 0.5 MeV for $\rho \approx \rho_{\rm eq}$. In addition, NSE predicts a composition characterized by free neutrons (with mass fraction $X_{\rm n} \sim 1 - Y_{\rm e}$), neutron-rich nuclei ($X_{\rm heavy} \sim Y_{\rm e}$) and a negligible amount of free protons, for initially low electron abundances ($Y_{\rm e} \lesssim 0.2$). Under these conditions, neutrino reactions are expected to be slower than the expansion time scale. In particular, the absorption of electron neutrinos on free neutron can increase $Y_{\rm e}$, but the rate is usually too slow to reach $Y_{\rm e,eq}$. Thus, we expect our two cases to bracket the actual evolution of the electron fraction.

Figure 4 shows the mass distribution of the electron fractions for all tracers at $t_{\rm init}$, for case A. Due to the initial high densities and low temperatures of the tracers, the average $Y_{\rm e}$ is rather low ($\langle Y_{\rm e} \rangle \approx 0.12$) and close to the values obtained in the simulation without the inclusion of weak reactions.

3.1. Nuclear network

In order to determine the composition of the fluid along the trajectories, we employ a complete nuclear reaction network (Winteler et al. 2012, Korobkin et al. 2012, Martin et al. 2015). It includes over 5800 nuclei between the valley of stability and the neutron drip line, comprising isotopes from H to Rg. The nuclear properties (e.g., mass excess, ground state spin, and partition functions) and reaction rates are taken from the compilation of Rauscher & Thielemann (2000) and Rauscher (2003) for the Finite Range Droplet Model (FRDM, Möller et al. 1995). In particular, the reaction rates are tabulated as the coefficients of a fit function in the JINA REACLIB format (Cyburt et al. 2010). Theoretical weak interaction rates including neutrino absorption on nucleons are taken into account (Fuller et al. 1982*a*, Fuller et al. 1982*b*, Fuller

et al. 1985, Langanke & Martínez-Pinedo 2001, Möller et al. 2003), and to compute them we utilize chemical potentials from the Helmholtz equation of state (Timmes & Swesty 2000). Furthermore, neutron capture for nuclei with $Z > 83$ and neutron-induced fission rates are taken from Panov et al. (2010) while beta-delayed fission probabilities are from Panov et al. (2005).

We feed the reaction network with the temporal profiles of the matter density and radial position obtained by post-processing the ejected tracers, see Sec. 3. The electron fraction, temperature, and nuclear composition are only initialized and then evolved consistently by the network. This ensures a smooth transition between the two different post-processing steps. As starting point of the Y_e and nucleosynthesis calculations, we still consider NSE conditions occurring at $T \approx 8$ GK. These conditions typically occur a few tens of milliseconds after the shock has reheated the outflow. From then on, we switch to the full reaction network to determine the nucleosynthesis, while descending to lower temperatures and densities. For temperatures below 3 GK, we further extrapolate the expansion inside the network assuming a homologous outflow. The energy generation by the r-process is calculated and its impact on the entropy is included (Freiburghaus et al. 1999, Korobkin et al. 2012) The heating mainly originates from beta decays and we assume that the energy is roughly equally distributed between thermalizing electrons and photons, and escaping neutrinos and photons (see Metzger et al. 2010, Barnes et al. 2016) for a recent discussion. We compute the final abundances at 10^9 years.

4. Results

4.1. Representative tracers

Both the shock and the neutrino irradiation have a strong effect on the electron fraction evolution. In the following, we examine how the considered reactions influence the electron fraction in detail.

In the upper panels of Figure 5, we show the hydrodynamical properties of two representative tracers, initialized according to case A. One tracer (left panel) starts with a density of $10^{12}\,\mathrm{g\,cm^{-3}}$ and an initial weak equilibrium electron fraction of 0.16. In the other tracer (right panel), the initial density is below $10^{12}\,\mathrm{g\,cm^{-3}}$ and the initial Y_e is assumed to be 0.044 (see Sec. 3). The former tracer is also representative of the trajectories initialized according to case B. A more extensive discussion about the differences between case A and B will be provided in Sec. 4.2. The lower panels illustrate the reaction rates calculated with Eqs. (19)−(22) as well as the resulting evolution of the electron fraction as a function of time. When the tracer leaves the neutrino diffusion regime, the relatively low temperatures favor the formation of neutron-rich, tightly bound nuclei in combination with free neutrons in NSE. Particularly, the abundance of free protons vanishes under such cold, neutron-rich conditions (cf. Sec 3). Electron neutrino absorption on free neutrons increases the electron fraction, despite the non-

negligible effect of Pauli blocking for the degenerate electrons in the final state. As the density decreases and the temperature increases, nuclei are more and more dissociated into free nucleons in NSE. After about 1 ms, a shock sets in and the sudden rise of temperature triggers electron captures and, to smaller extent, positron captures. Hence, the electron fraction drops sharply. As soon as the temperature decreases, as a consequence of the expansion induced by the shock itself, the subsequent evolution is mainly determined by electron neutrino captures on neutrons. When material expands to larger distances, the (anti)neutrino fluxes fade as R^{-2} and the electron fraction flattens after a few milliseconds. In the subsequent expansion phase, density and temperature decrease monotonically, until leaving NSE and reaching conditions relevant for the r-process nucleosynthesis.

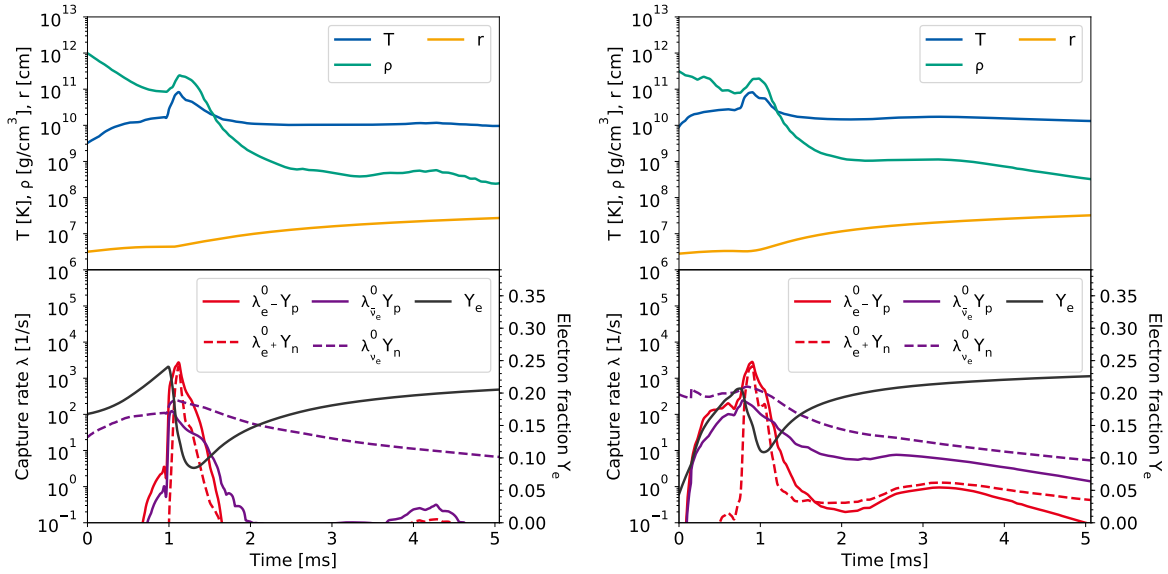

Figure 5. Temporal evolution for two selected tracers of case A with high isotropic luminosities. The left panel shows a tracer with $Y_{\rm e,ini} = 0.044$, while the right panel shows a tracer starting from beta-equilibrium conditions with $Y_{\rm e,ini} \sim 0.16$. Top panels: hydrodynamic properties of a representative tracer. Bottom panels: trends of the considered reaction rates and evolution of the electron fraction over time. Rates that lead to a decrease in the electron fraction are shown with solid lines, while rates that cause an increase of the electron fraction are plotted with dashed lines.

It is instructive to discuss the effects of the shock passage on the electron fraction in terms of the different conditions experienced in the density-temperature plane. Since (anti)neutrino capture rates, λ_{ν_e} and $\lambda_{\bar{\nu}_e}$, are weakly affected by density and temperature gradients in the free-streaming regime, we restrict our discussion to the electron and positron captures. Using Eqs. (19) and (20), we evaluate the rates for a large sample of density and temperature conditions. To present their impact on the evolution of the electron fraction, we consider the product of the rates and the corresponding target abundance, i.e., $\lambda_x Y_x$. The nucleon abundances are calculated for NSE conditions with the aid of the nuclear EOS. Figure 6 shows with contour lines the conditions where

electron and positron captures balance each other, $\lambda_{e^-} Y_p / (\lambda_{e^+} Y_n) = 1$. The contour lines are labeled with the corresponding electron fraction and illustrate a range of Y_e between 0.05 and 0.30 in steps of $\Delta Y_e = 0.05$. For a given Y_e, in the region above the corresponding line electron captures dominate, while positron captures win for lower densities or larger temperatures. This plane can be understood in terms of the degree of degeneracy of the electrons. Making use of the approximated expressions of the rates derived in Appendix A, we obtain:

$$\frac{\lambda^0_{e^-} Y_p}{\lambda^0_{e^+} Y_n} \approx \frac{F_4\left(\eta_e - \frac{\Delta}{k_B T}\right) Y_e}{F_4(-\eta_e)\,(1 - Y_e)}\,, \tag{26}$$

where η_e is the electron degeneracy parameter, defined as $\eta_e \equiv \mu_e / k_B T$, μ_e the relativistic electron chemical potential including the rest mass. We have also assumed that temperature is high enough to dissociate most of the nuclei in free nucleons. When electrons are degenerate (i.e., for high densities and low temperatures), $\eta_e \gg 1$ and $F_4(\eta_e - \Delta/(k_B T))/F_4(-\eta_e) \sim (\eta_e - \Delta/(k_B T))^5 e^{\eta_e}/120 \gg 1$ (Bludman & van Riper 1977, Takahashi et al. 1978). On the contrary, in non-degenerate conditions $\eta_e \sim 0$ and $F_4(\eta_e - \Delta/(k_B T))/F_4(-\eta_e) \sim [1 + 0.974\,(\eta_e - \Delta/(k_B T))]$. Thus, for high temperatures and/or low densities such that $\mu_e \lesssim \Delta$, the positron capture rate becomes dominant. More in general, for $\mu_e \lesssim \Delta/2$ the rates become comparable for all regimes.

We evolve again the tracer from the left panels of Figure 5, but including only electron and positron captures in Eqs. (16) and (17). We show the subsequent evolution of its Y_e with a colored thick line in Figure 6. Its color changes according to the evolution of the electron fraction and coherently with the thin threshold lines. When the ejecta are

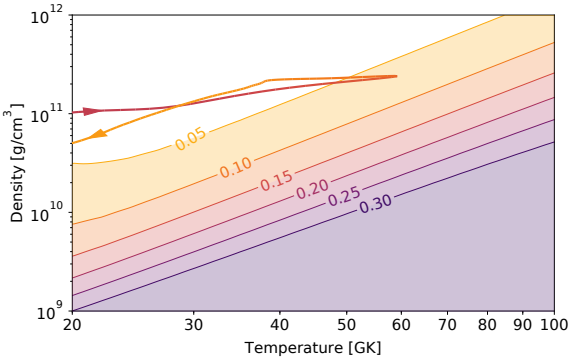

Figure 6. Comparison of the electron and positron captures for different conditions in the density-temperature plane. The thick line shows the electron fraction evolution along the representative trajectory from Figure 5 including only electron and positron captures. Arrows indicated the temporal evolution of the hydrodynamics along the trajectory. The thin lines in the colored area mark critical values of density and temperature, labeled with the corresponding electron fraction in NSE. These are the conditions at which the electron capture rate equals the positron capture rate, i.e., $\lambda^0_{e^-} Y_p / (\lambda^0_{e^+} Y_n) = 1$. At higher densities, electron capture dominates, while at lower densities positron captures win. Note that we only show contour lines for electron fractions up to $Y_e = 0.30$.

hit by the shock, the electron fraction of the trajectory is close to the weak-equilibrium value, $Y_e \approx 0.16$, given no (anti)neutrino absorption. For the high degeneracy conditions experienced at the shock passage, electron captures are initially favored by a factor of ~ 100 over positron captures. As the temperature increases toward the peak value, the electron degeneracy decreases and this factor goes down, but not enough to make positron captures dominant. Instead, the ongoing electron captures rapidly decrease the electron fraction, shifting the line of $\lambda^0_{e^-} Y_p / \left(\lambda^0_{e^+} Y_n\right) = 1$ into the direction of the conditions found for the trajectory. This effectively flattens the evolution of the electron fraction, as it tends to balance the capture rates. At the shock peak, the reaction rates are fast enough to reach the corresponding weak equilibrium conditions. When the electron fraction has dropped to $Y_e \approx 0.07$, the ratio of electron and positron capture rates is close to unity. However, the temperature is already very low at this point, shutting off both kinds of captures. If these reaction types were the only ones involved in the electron fraction evolution, then its profile would remain constant at later times.

4.2. Property distributions

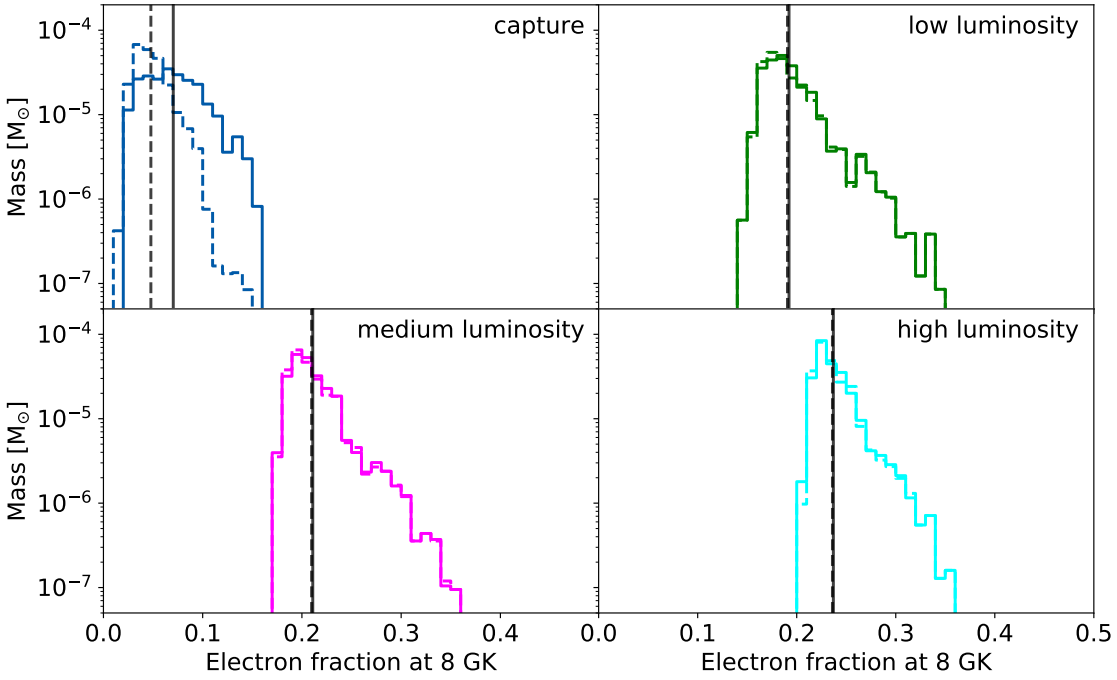

Figure 7. Mass distributions of the electron fraction at 8 GK obtained from the post-processed tracers. Different panels refer to different treatments of the weak reactions. In the top-left panel, we include only electron and positron captures, while in the other panels also (anti)neutrino captures with increasing, isotropic luminosities. Solid and dashed lines refer to the results obtained using case A and case B as initial conditions, respectively. Vertical lines mark the average electron fractions. In all cases, we obtain a rather broad distribution of the electron fraction, with generally less neutron-deficient values, as we assume higher (anti)neutrino luminosities.

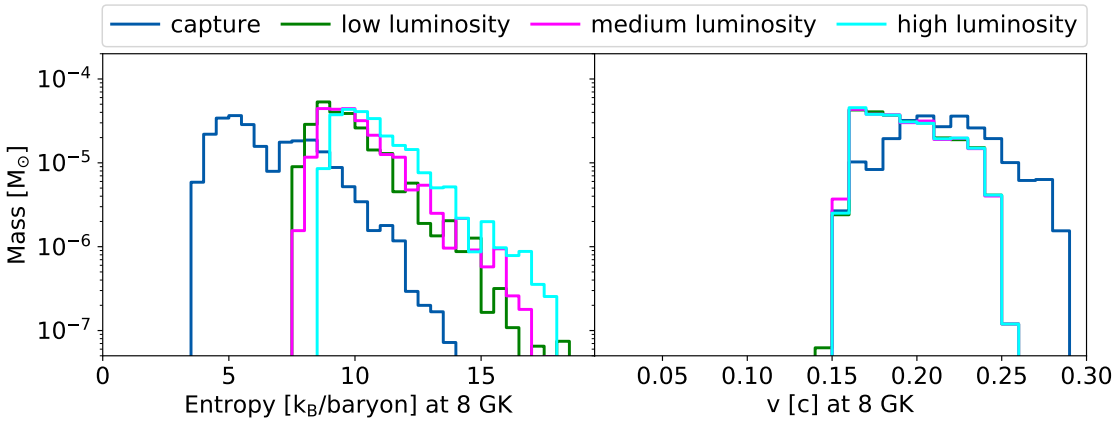

Figure 8. Mass distributions of the entropy (left) and radial velocity (right) at 8 GK, obtained by evolving ejected tracers initialized according to case A. Different colors refer to different treatments of the weak reactions, while neutrino luminosities are assumed to be isotropic (cf. Figure 7).

The nucleosynthesis in the ejecta is sensitive to the electron fraction, $Y_{\rm e}$, the entropy, s, and the expansion time scale (or equivalently the expansion velocity, $v_{\rm 8GK}$) at NSE freeze-out (e.g., Hoffman et al. 1997). Using the whole ensemble of ejected tracers from the simulation, we obtain distributions for all these quantities, recorded when the tracer temperature drops below 8 GK, well after the shock has passed. At later time, weak processes can still change $Y_{\rm e}$ and s. However, due to the low temperatures and large distances from the remnant ($R \gtrsim 600\,$km), these residual variations are small ($\delta Y_{\rm e}/Y_{\rm e} \sim 0.02$ and $\delta s/s \sim 0.015$).

In Figure 7, we present the electron fraction distributions for different treatments of the weak reactions (different panels) and for both cases A and B (with solid and dashed lines, respectively). If we only include electron and positron captures to evolve the tracers (top-left panel)‖, different initial conditions results in different $Y_{\rm e}$ distributions. In particular, the broader and less neutron-rich initial distribution assumed in Case A is reflected in the evolved distribution at 8 GK. A closer comparison reveals that in this case the peak and the mass-weighted average are located around $Y_{\rm e} = 0.07$, thus reduced compared to the beta-equilibrium values obtained at weak freeze-out (cf., Figure 4). In the absence of neutrino captures, the electron fraction is not significantly modified after being processed by the shock wave. This is a direct consequence of the effect of the shock passage discussed in Sec. 4.1. As soon as the temperature increases due to the shock passage, electron and positron captures are significantly enhanced (cf., Figure 5). In Figure 9, we show the electron fraction in neutrinoless beta-equilibrium on the matter density-entropy plane. The white ellipse contains the hydrodynamical conditions experienced by most of the tracers at the shock peak and shows that the resulting equilibrium $Y_{\rm e}$ scatters around $Y_{\rm e} \sim 0.10$ for most of the ejecta. In case B,

‖ We notice that this treatment of the weak reactions is equivalent to what is done in simulations employing leakage schemes without absorption terms in the optically thin regime.

the lower initial Y_e values (~ 0.044) favor positron captures, which increase the electron fraction towards the equilibrium conditions, where $\lambda^0_{e^-} Y_p / \left(\lambda^0_{e^+} Y_n\right) = 1$. However, due to the vicinity of the initial electron fraction to the equilibrium one, and to the relatively slow positron capture rate ($\lambda^0_{e^+} Y_n \, \Delta t_{shock} \lesssim 1$, where $\Delta t_{shock} \approx 0.5\,$ms is the width of the shock duration), the resulting rise in Y_e is only marginal and the electron fraction distribution peaks again around $Y_e = 0.05$. On the contrary, ejecta in case A start often with a considerably higher weak equilibrium electron fraction (see Figure 4). The conditions at the shock peak are relatively far from the $\lambda^0_{e^-} Y_p / \left(\lambda^0_{e^+} Y_n\right) = 1$ line, and electron capture is enhanced by electron degeneracy up to two orders of magnitude with respect to positron capture. Moreover, weak reactions are fast enough to approach equilibrium, since for most of the trajectories $\lambda^0_{e^-} Y_p \, \Delta t_{shock} > 1$. This leads to an appreciable decrease in the electron fraction, compared to the initial conditions of case A, Figure 4, and at the same time to a qualitative different behavior compared to case B, where equilibrium at the shock is almost never reached.

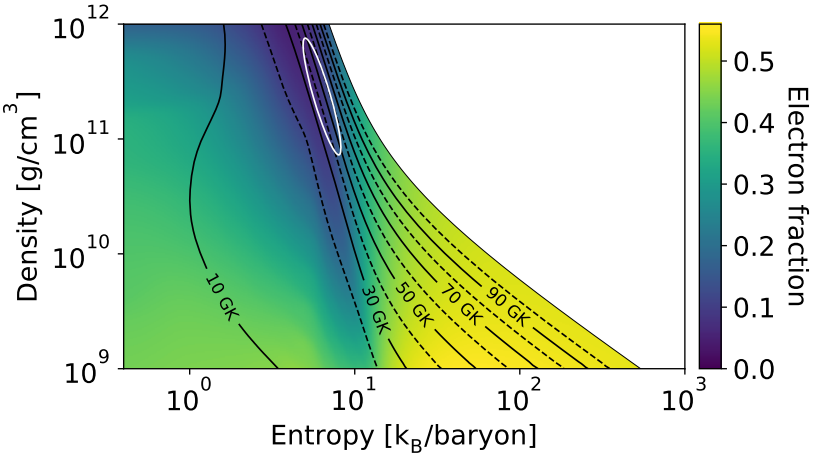

Figure 9. Beta-equilibrium values for the electron fraction in the entropy-density plane. Dashed and solid black lines indicate temperature contours. The white ellipse shows the one-sigma environment of the conditions that the tracers encounter at the peak temperature of the shock. Accordingly, the electron fraction tends to evolve toward an equilibrium value of $Y_e \sim 0.10$ if only electron and positron captures are considered.

The other panels of Figure 7 show the three cases including (anti)neutrino absorption reactions for different strength of the neutrino luminosities (see Table 1). We first consider the case of isotropic neutrino emission (i.e., $\alpha = 0$ in Eq. (3)). For all considered combinations, the late-time electron fraction is generally shifted to higher values, compared to the starting beta-equilibrium values. This is mainly a consequence of the neutrino absorption occurring after the passage of the shock wave. The mass-weighted average is contained within the range $0.19 \lesssim \langle Y_e \rangle \lesssim 0.23$ and larger neutrino fluxes result in higher $\langle Y_e \rangle$. The distributions have a tail toward high electron fractions, up to $Y_e \approx 0.36$ for all degrees of irradiation. Once neutrino absorptions are taken into account, the differences between case A and B vanish. This is due to copious

absorptions of electron neutrinos on neutrons, which occur before the shock passage and for both cases A and B. The subsequent increase in the electron fraction, well above $Y_{\rm e} \approx 0.10$, sets the tracer conditions similar to the ones we have discussed above, in the case of electron and positron captures alone and initial conditions in case A. Due to the achievement of the equilibrium $Y_{\rm e}$ inside the shock, the differences between the cases A and B disappear and the variety in the final distributions depends only on the degree of neutrino irradiation after the shock passage.

Since our results and conclusions are largely independent from the initial conditions, in the following we will consider only case A. The distributions for the entropy per baryon and for the asymptotic expansion velocity are presented in Figure 8. The passage of the shock wave increases the entropy from $\sim 4\ k_{\rm B}$ baryon^{-1} to $\sim 8\ k_{\rm B}$ baryon^{-1}. In the electron-positron capture case, the emission of neutrinos removes efficiently entropy from the fluid elements. The resulting distribution at 8 GK shows two peaks, one around $5\ k_{\rm B}$ baryon^{-1} and one around $7\ k_{\rm B}$ baryon^{-1}, which correlate with the peak temperature after the shock passage: the more intense neutrino emission from the hotter tracers ($T_{\rm peak} > 40$ GK) reduces the entropy more significantly than from the colder ones. If neutrino absorption processes are included, the captures of high energy (anti)neutrinos on expanding and cooling matter compensate the reduction of entropy provided by neutrino emission. The bimodal distribution observed before is substituted by a distribution with a single peak around $8-9\ k_{\rm B}$ baryon^{-1} and a rapidly decreasing tail, extending up to $16\ k_{\rm B}$ baryon^{-1}. Due to the balance between emission and absorption processes, we notice only a marginal increase in the entropy profiles for increasing neutrino luminosities. The ejecta expand with fast velocities ($v_{8\,\rm GK} > 0.15\ c$) in all cases. The wider and faster distribution obtained in the electron-positron capture case is simply a consequence of the more rapid cooling observed in this case. Once neutrino absorption processes are taken into account, the NSE freeze-out temperature $T_{\rm NSE} = 8\,\rm GK$) is reached at later times and larger radii. In these cases, the radial velocity of each fluid element has further decreased due to the motion inside the gravitational well, and has approached its asymptotic value, v_∞.

Finally, we compare the previous results, obtained assuming an isotropic ν emission (Eq. (3) with $\alpha = 0$), with the ones obtained in the anisotropic case (Eq. (3) with $\alpha = 2$). While the entropy and the expansion velocity show only minor variations, more interesting differences are visible in the electron fraction distributions, presented in Figure 10. Since most of the ejection happens inside a solid angle delimited by a polar angle $\theta = \pi/2 \pm \pi/6$ about the equatorial plane, the assumption of an anisotropic neutrino emission decreases the neutrino fluxes experienced by the escaping matter and lower the effect of electron neutrino absorption. This results in systematically more neutron-rich ejecta, with electron abundances usually decreased by $\sim$15% and average values located between $\langle Y_{\rm e} \rangle \approx 0.16$ (low luminosity) and $\langle Y_{\rm e} \rangle \approx 0.21$ (high luminosity). Our results suggest also that, in the case of ejecta emitted closer to the polar axis, a high degree of anisotropy in the neutrino emission could result in a large increase of the electron fraction inside the polar region.

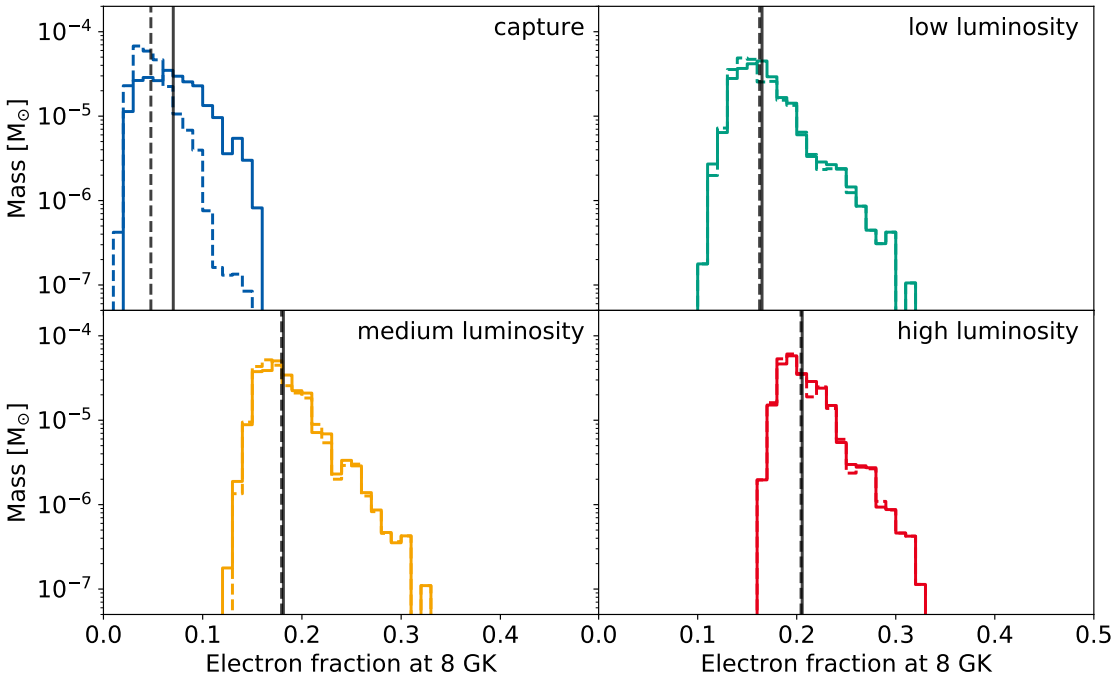

Figure 10. Same as in Figure 7, but for anisotropic neutrino luminosities.

4.3. Nucleosynthesis yields

Having post-processed the ejected tracers for obtaining an updated electron fraction evolution, we use the outcome as an input for subsequent nucleosynthesis calculations. The nucleosynthesis yields are shown in Figure 11, alongside with the solar r-process abundances (dots, Lodders 2003). We first consider the isotropic luminosity case, $\alpha = 0$ in Eq. (3). Gray lines represent the abundance patterns of individual tracers, while colored lines the abundances summed over all tracers. For a straightforward comparison, we apply the same colors as for the electron fraction distributions in Figure 7. In the case with only electron and positron captures, we find a robust r-process nucleosynthesis from second to third peak due to the extremely neutron-rich conditions. Moreover, the abundances of individual tracers are close to the average one, with a small spread reflecting the narrow distribution in electron fraction. In contrast, the three remaining cases including neutrino captures show a rather strong dependence on the neutrino irradiation flux, and the larger spreads in the electron fraction distribution translate in a larger variety behaviors of the single tracers with respect to the average one. The component of the ejecta with relatively high electron fraction forms r-process nuclei up to the second peak. When these ejecta are complemented by a neutron-rich component, the mass-integrated nucleosynthesis almost ranges from the first to the third r-process peak. The relative importance of the light to the heavy r-process nuclei depends on the increase in electron fraction and, in turn, on the intensity of the neutrino luminosities. The first peak is somewhat underproduced in the case with low luminosities. Increasing the (anti)neutrino luminosities has two effects. First, the abundances of nuclei up to

the second r-process peak are enhanced. Second, the abundances of heavy nuclei with $A \gtrsim 130$ decrease by up to more than an order of magnitude with respect to the solar abundances. In the high luminosity case, the increase of the electron fraction peak above 0.23, combined with a rather low matter entropy, prevents a significant production of r-process nuclei above the second peak.

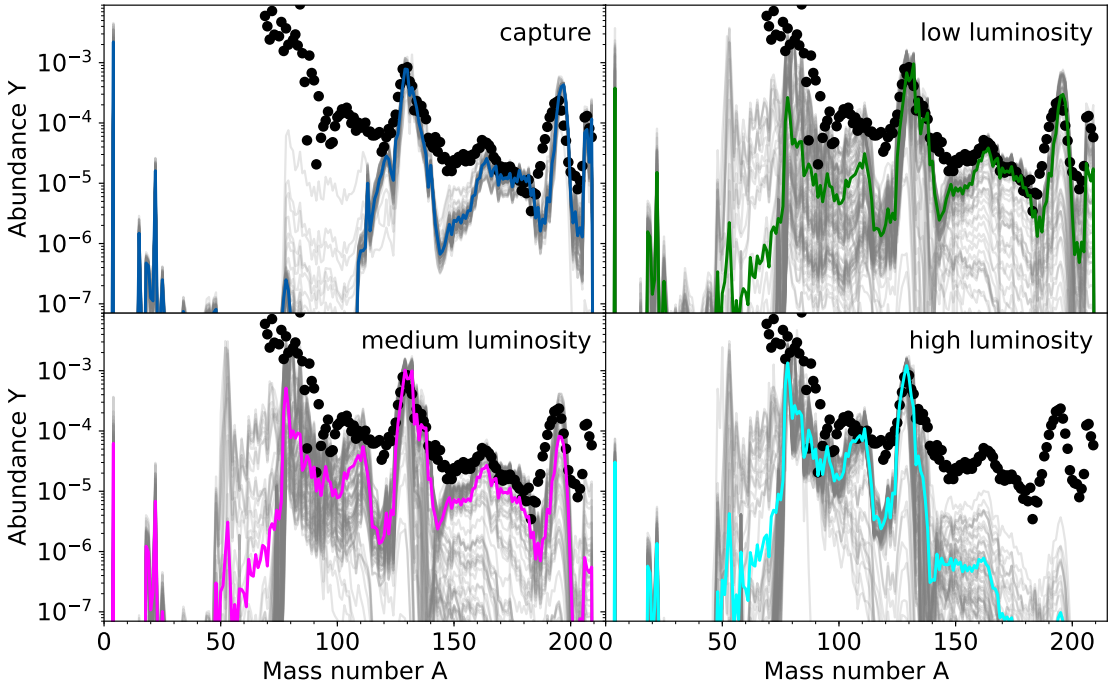

Figure 11. Nucleosynthesis yields when including weak reactions. We find a robust r-process for the case including only electron and positron captures. However, the abundances for heavy nuclei with ($A \gtrsim 130$) decreases and the ones for lower mass nuclei ($A \lesssim 130$) increases if higher (anti)neutrino luminosities are assumed. Color scheme and luminosity cases are the same as in Figure 7. Gray lines show the abundance pattern of individual tracers. Solar r-process abundances are shown as red dots.

The angular dependence of the (anti)neutrino luminosities also affects the r-process nucleosynthesis in the dynamic ejecta. In Figure 12, we present the final abundance yields obtained in the case of anisotropic neutrino emission, $\alpha = 2$ in Eq. (3), again in comparison with the solar r-process abundances (dots, Lodders 2003). Since the dynamic ejecta are mainly ejected close to the equatorial plane, the shadow effect of the forming disk reduces the neutrino fluxes that irradiate the expanding matter. Similar to the isotopic cases, a weak component that comprises nuclei with $A \lesssim 130$ is coproduced. As a consequence, this reduces the abundances in the region beyond the second r-process peak, but not as much as in the cases exhibiting isotropic luminosity. On the contrary, we find a rather robust r-process pattern, which underproduces the rare-earth peak and the third peak by up to a factor of ~ 2 for the highest assumed (anti)neutrino luminosities. All yields are complemented by lighter heavy elements between the first

and the second peak.

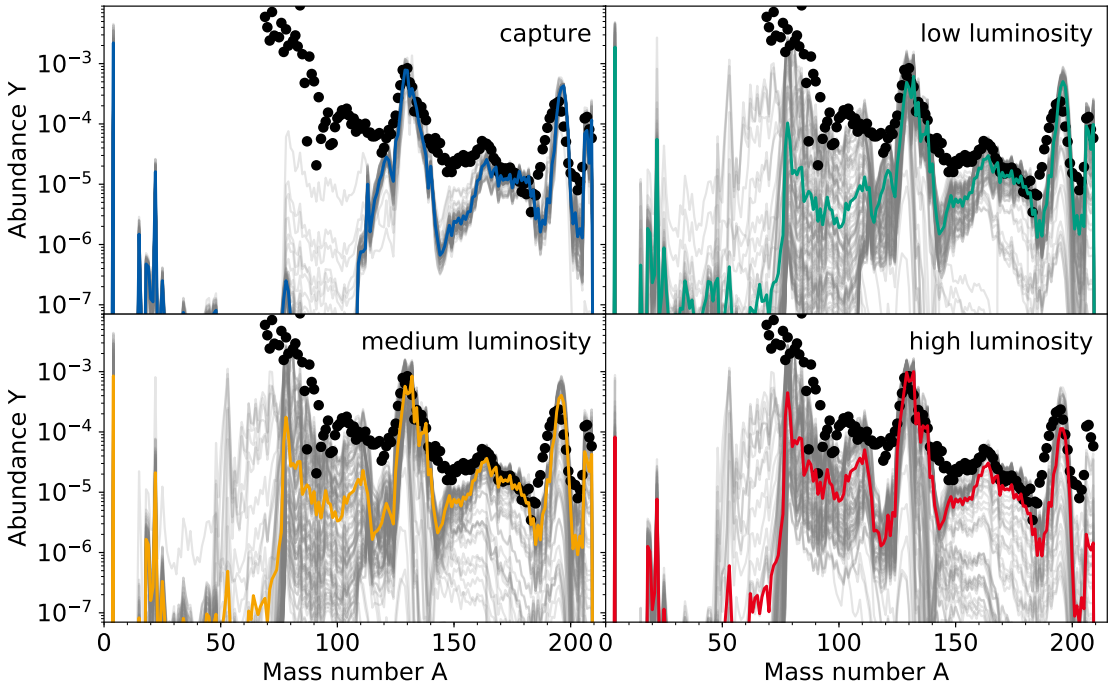

Figure 12. Nucleosynthesis yields when including weak reactions and angle dependent luminosities. Color scheme and luminosity cases are the same as in Figure 10.

4.4. Discussion and comparison

Our work extends on the results of previous studies (e.g., Roberts et al. (2017) and, in particular, Goriely et al. (2015)). Goriely et al. (2015) report a similar initial¶ electron fraction distribution as we do ($0.0 \lesssim Y_\mathrm{e} \lesssim 0.2$). However, they find a peaked instead of a bimodal distribution, and their distribution extends to $Y_\mathrm{e} = 0.3$. Particularly when solely considering electron and positron captures in the subsequent evolution of Y_e, they find a very broad distribution, and this is because of to the occurrence of a shock at larger densities and much larger temperatures ($T \gtrsim 100\,\mathrm{GK}$). In their cases including (isotropic) neutrino irradiation, the relatively large (neutrinoless) weak equilibrium Y_e occurring at weak freeze-out is further increased by ν_e and positron absorptions. Thus, when including also neutrino captures on nucleons, they report on higher electron fractions than we find in our results, even up to $Y_\mathrm{e} = 0.5$ (though this is likely also due to the different treatment of λ_ν^k). Their corner case for decreased temperatures ($T/3$) is comparable to our results, since the temperatures are similarly high here. The lower shock temperature generally implies a milder decrease of Y_e during the shock, and therefore more emphasized effects of ν_e and $\bar{\nu}_\mathrm{e}$ captures, leading to an overall higher $\langle Y_\mathrm{e} \rangle$ at late times. When only taking into account electron and positron

¶ For beta-equilibrium conditions at $\rho_\mathrm{eq} = 10^{12}\,\mathrm{g\,cm^{-3}}$.

captures, they find a distribution that is very similar to our corresponding case. Overall, our results confirm their conclusion that the r-process nucleosynthesis shows a robust abundance pattern, unless the neutrino flux is extraordinarily high (see our case "high luminosity"). Nevertheless, the weak r-process component with mass numbers $A \lesssim 130$ is affected by the degree of weak interactions, i.e., the larger the neutrino flux the more the ejecta yield nuclei below the second r-process peak. Under the assumptions made here, there are always admixtures of these two distinct components and there is a trade-off to produce either of the two. Therefore, we need at least a second kind of ejecta to explain the full r-process pattern from the first to the third r-process peak (see, e.g., Hansen et al. 2014).

For the merger of a black hole and a neutron star, Roberts et al. (2017) investigate the impact of neutrinos on the nucleosynthesis. It is important to note that such a system lacks an interaction region, hence the ejecta originate from the tidal tails. This component is extremely neutron-rich and cold enough for electron and positron captures to be neglected. Due to the rapid outflow timescales of the ejecta, Roberts et al. (2017) find that the electron fraction distribution is not shifted significantly. Even for their highest (isotropic) luminosity case ($L_{\nu_\mathrm{e}} = 2.5 \cdot 10^{53}\,\mathrm{erg/s}$, $L_{\bar{\nu}_\mathrm{e}} = 1.5 L_{\nu_\mathrm{e}}$), the electron fraction obeys $Y_\mathrm{e} \lesssim 0.25$. Similar to our results, the heavy elements from the second to the third r-process peak are produced robustly, with subtle enhancements for the abundances of nuclei with $A \lesssim 130$ due to neutrino irradiation.

Furthermore, GR radiation-hydrodynamics simulations also found that Y_e in the dynamic ejecta of BNS mergers can be significantly enhanced by weak reactions (e.g., Sekiguchi et al. 2015, Foucart et al. 2015, Radice et al. 2016). However, Sekiguchi et al. (2015) reported that the inclusion of neutrino absorption in optically thin conditions has a minor impact on the average electron fraction of the ejecta in their models. These could be explained by the occurrence of the shock at lower electron degeneracy conditions (i.e., at lower densities and/or higher temperatures), favoring positron captures on neutrons, rather than electron captures on protons (see, for example, Figure 6).

5. Conclusion

In this paper, we have explored the impact of weak reactions on the distributions of the electron fraction and of the entropy in the ejecta obtained from an equal mass neutron star binary merger simulated in full GR, with a finite temperature, microphysical EOS. We have focused on the shock-heated ejecta that originates from the disk. We have used a parameterized post-processing treatment that allowed us to explore consistently the impact of individual reactions on Y_e and on the entropy. It also permitted to disentangle the role of some of the most relevant aspects influencing the electron fraction evolution, including the impact of shock heating, the dependence on the intensity of the integrated neutrino luminosities, and on the degree of anisotropy in the neutrino emission. For each model, we have computed detailed nucleosynthesis yields, relating the impact of weak reactions to the properties of the synthesized nuclear abundances.

These are our three major findings:

1.) The inclusion of neutrino absorption on free nucleons, in addition to neutrino emission from electron and positron absorptions, changes significantly the properties of the ejecta. Even if electron antineutrino luminosity initially dominates over electron neutrino luminosity, the neutron abundance and the larger reaction Q-value favor electron neutrino absorption on neutrons for all the tested luminosities, increasing always the electron fraction. The larger the neutrino luminosities are, the larger the increase in $Y_{\rm e}$ distribution is. Moreover, the increase in matter entropy due to the absorption of neutrinos roughly compensate the decrease due to neutrino emission.

2.) The occurrence of a shock in the ejection process does not necessarily lead to an increase of the electron fraction in neutron-rich matter. If the shock occurs at densities $\gtrsim 10^{11}\,{\rm g\,cm^{-3}}$ and temperatures $\lesssim 8\,{\rm MeV}$, electron degeneracy favors electron captures on protons rather than positron captures on neutrons, for an initial $Y_{\rm e} > 0.10$. For the examined trajectories, when the peak temperature in the shock exceeds $\sim 5\,{\rm MeV}$ and $Y_{\rm e} > 0.1$, electron captures are fast enough to reach weak equilibrium around $Y_{\rm e} \approx 0.10$. This has the remarkable consequence that the subsequent evolution becomes independent from the thermodynamical history before the shock. On the other hand, if $Y_{\rm e} < 0.1$ before the shock occurs, positron absorption is not fast enough to ensure equilibrium. In our tracer sample, the latter condition is verified only when neutrino absorption is neglected. Otherwise, neutrino absorption increases always $Y_{\rm e}$ above 0.1 before the shock occurrence.

3.) Neutrino absorption is proportional to the local neutrino flux. Thus, in addition to the total luminosity and energy spectrum, the angular dependence of the neutrino luminosity, in combination with the spatial distribution of the ejecta, has a relevant impact. Since the shock heated ejecta that we have analyzed in our work expand close to the equatorial plane, a significant degree of anisotropy in the neutrino emission can lead to appreciable differences in the $Y_{\rm e}$ distributions, compared with the isotropic case.

Our work confirms previous findings that weak reactions are crucial to set the properties of the ejecta in binary compact mergers, even for the dynamic ejecta (Wanajo et al. 2014, Sekiguchi et al. 2015, Goriely et al. 2015, Sekiguchi et al. 2016, Radice et al. 2016, Roberts et al. 2017). Thus, future studies that aim at exploring the properties of the ejecta and address the problem of the related nucleosynthesis will require a careful inclusion of neutrino physics, both in terms of the relevant neutrino reactions and of the characteristic emission properties. The detailed results we have obtained are intrinsically related with the specific properties of the tracer particles we have used in our analysis. Some of our findings might not apply to shock-heated ejecta that significantly differ from ours. However, we have shown that our approach is useful to investigate the origin of the increase in $Y_{\rm e}$ in decompressed neutron-rich matter from binary compact mergers, as well as the relevance of single reactions. Moreover, it is

well suited to analyze the results of detailed radiation-hydrodynamical simulations with a controlled and inexpensive approach, in particular to explore in details the different thermodynamical conditions experienced by fluid elements during a binary merger. A larger and more detailed set of models is required to extensively explore the different conditions experienced by matter and radiation during compact mergers.

Acknowledgments

The authors thank L. Roberts, and D. Radice for useful discussions. A. A., D.M. and A. P. acknowledge support from the Helmholtz-University Investigator grant No. VH-NG-825, from the BMBF under grant No. 05P15RDFN1, and from the European Research Council Grant No. 677912 EUROPIUM. A. P. and D. M. thank the GSI Helmholtzzentrum für Schwerionenforschung GmbH for the usage of computational resources. The simulations with the `FISH+ASL` code were supported by a grant from the Swiss National Supercomputing Centre (CSCS) under project ID 667.

Appendix A. Weak magnetism and recoil corrections. Approximated captures rate expressions.

In Eqs. (19)−(22), we employ the weak magnetism and recoil corrections provided by Horowitz (2002) for charged current reactions on free nucleons:

$$\mathcal{R}_\nu(E) = \frac{1}{c_v^2+3c_a^2}\frac{1}{(1+2x)^3}\left[c_v^2\left(1+4x+\frac{16}{3}x^2\right)+3c_a^2\left(1+\frac{4}{3}x\right)^2 \right.$$
$$\left. \pm 4\,(c_v+F_2)\,c_a x\left(1+\frac{4}{3}x\right)+\frac{8}{3}c_v F_2 x^2+\frac{5}{3}x^2\left(1+\frac{2}{5}x\right)F_2^2\right]. \quad \text{(A.1)}$$

In the above expression, $x = E/(M_\mathrm{b}c^2)$, M_b is the baryon mass, $c_v = 1$, $c_a = g_a \approx 1.26$, and $F_2 \approx 3.706$. The upper sign refers to ν_e, the lower to $\bar{\nu}_\mathrm{e}$.

In our calculations, we did not consider any approximations to the rates, while in the following, starting from Eqs. (19)−(22), we derive approximated expressions in the form:

$$\lambda_x^0 = c\; n_x\; \langle\sigma_x\rangle\,, \quad \text{(A.2)}$$

where n_x is the target density and $\langle\sigma_x\rangle$ an average cross section. This derivation is useful to provide simpler expressions for the rates and to compare with others used in the literature. We neglect both the electron rest mass correction ($\mathcal{M} \to 1$ and $\Delta + m_\mathrm{e} \to \Delta$ in the non-vanishing lower limits of integration) and the Pauli blocking factors involving electrons and positrons in the final state. Moreover, since for typical neutrino energies $x \ll 1$, we expand Eq. (A.1) in powers of x:

$$\mathcal{R}_\nu(E) \approx 1 - 2x\frac{(5c_a^2 \mp 2c_a\,(c_v+F_2)+c_v^2)}{(c_v^2+3c_a^2)} +$$
$$\frac{1}{3}x^2\frac{(88c_a^2 \mp 56c_a\,(c_v+F_2)+5F_2^2+8c_vF_2+16c_v^2)}{(c_v^2+3c_a^2)}+\mathcal{O}(x^3)\,. \quad \text{(A.3)}$$

In the case of (anti)neutrino capture rates, $\lambda^0_{\nu_e}$ and $\lambda^0_{\bar{\nu}_e}$, we assume the free streaming radiation to propagate mainly radially, and its spectrum to be described by a Fermi-Dirac distribution with vanishing degeneracy parameter and mean energy $\langle E_\nu \rangle = k_B T_\nu F_3(0)/F_2(0)$. For the corresponding capture rates, we obtain

$$\lambda^0_{\nu_e} = c\, n_{\nu_e}\, \langle \sigma_{\nu_e} \rangle \,, \tag{A.4}$$

$$\lambda^0_{\bar{\nu}_e} = c\, \tilde{n}_{\bar{\nu}_e}\, \langle \sigma_{\bar{\nu}_e} \rangle \,. \tag{A.5}$$

In the above expressions, n_{ν_e} is the electron neutrino particle density, which can be expressed in terms of the local radial flux, Eq. (3), while $\tilde{n}_{\bar{\nu}_e}$ is a modified expression of the electron antineutrino particle density, which takes into account the non-zero lower integration limit:

$$n_{\nu_e} = \frac{\mathcal{F}_{\nu_e}}{c} \,, \tag{A.6}$$

$$\tilde{n}_{\bar{\nu}_e} = \frac{\mathcal{F}_{\bar{\nu}_e}}{c} \frac{F_2(-\Delta/k_B T_{\bar{\nu}_e})}{F_2(0)} \,. \tag{A.7}$$

$F_k(\eta)$ is the Fermi integral of order k and argument η.

The average cross sections $\langle \sigma_\nu \rangle$ are then computed by inserting Eq. (A.3) up to the first order in x inside Eqs. (21) and (22), and then averaging over the neutrino distribution functions:

$$\langle \sigma_\nu \rangle \approx \frac{\sigma_0}{(m_e c^2)^2} \langle \epsilon_\nu^2 \rangle \left\{ \left[1 + 2\frac{\Delta \langle \epsilon_\nu \rangle}{\langle \epsilon_\nu^2 \rangle} + \frac{\Delta^2}{\langle \epsilon_\nu^2 \rangle} \right] + \right.$$
$$\left. - (\gamma \mp \delta) \left[\frac{\langle \epsilon_\nu^3 \rangle}{\langle \epsilon_\nu^2 \rangle M_b c^2} + 2\frac{\Delta}{M_b c^2} + \frac{\Delta^2 \langle \epsilon_\nu \rangle}{\langle \epsilon_\nu^2 \rangle M_b c^2} \right] \right\} \,, \tag{A.8}$$

In Eq. (A.8), the upper sign is for ν_e while the lower sign for $\bar{\nu}_e$, $\gamma = 2\,(c_v^2 + 5c_a^2)\,/\,(c_v^2 + 3c_a^2)$, and $\delta = 4c_a^2\,(c_v + F_2)\,/\,(c_v^2 + 3c_a^2)$. We compute the neutrino and antineutrino energy moments via

$$\left\langle \epsilon^n_{\nu_e} \right\rangle = (k_B T_{\nu_e})^n \, \frac{F_{n+2}(0)}{F_2(0)} \,, \tag{A.9}$$

$$\left\langle \epsilon^n_{\bar{\nu}_e} \right\rangle = (k_B T_{\bar{\nu}_e})^n \, \frac{F_{n+2}(-\Delta/(k_B T_{\bar{\nu}_e}))}{F_2(-\Delta/(k_B T_{\bar{\nu}_e})} \,, \tag{A.10}$$

where we took again into account the lower integration limit by modifying the neutrino degeneracy parameter.

In the case of electron and positron captures on nucleons, the rates are expresses as

$$\lambda^0_{e^-} = c\, \tilde{n}_{e^-}\, \langle \sigma_{e^-} \rangle \,, \tag{A.11}$$

$$\lambda^0_{e^+} = c\, n_{e^+}\, \langle \sigma_{e^+} \rangle \,. \tag{A.12}$$

In the previous expressions, n_{e^+} is the positron particle density while $\tilde{n}_{e^-}$ is a modified version of the electron particle density,

$$n_{e^-} = \frac{8\pi}{(2\pi\hbar c)^3} (k_B T)^3 \, F_2 \left(\frac{\mu_e - \Delta}{k_B T} \right) \,, \tag{A.13}$$

$$n_{e^+} = \frac{8\pi}{(2\pi\hbar c)^3} (k_B T)^3 \, F_2 \left(-\frac{\mu_e}{k_B T} \right) \,, \tag{A.14}$$

where $\mu_{\rm e}$ is the relativistic electron chemical potential, and we used the fact that for high enough temperatures $\mu_{\rm e^+} = -\mu_{\rm e}$. The average capture cross-sections for electrons and positrons, $\langle\sigma_{\rm e^-}\rangle$ and $\langle\sigma_{\rm e^+}\rangle$, are given by:

$$\langle\sigma_{\rm e}\rangle \approx \frac{\sigma_0}{2\left(m_{\rm e}c^2\right)^2}\left\langle\epsilon_{\rm e}^2\right\rangle\left\{\left[1+2\frac{\Delta\langle\epsilon_{\rm e}\rangle}{\langle\epsilon_{\rm e}^2\rangle}+\frac{\Delta^2}{\langle\epsilon_{\rm e}^2\rangle}\right]+\right.$$
$$\left.-\left(\gamma\mp\delta\right)\left[\frac{\langle\epsilon_{\rm e}^3\rangle}{\langle\epsilon_{\rm e}^2\rangle M_{\rm b}c^2}+2\frac{\Delta}{M_{\rm b}c^2}+\frac{\Delta^2\langle\epsilon_{\rm e}\rangle}{\langle\epsilon_{\rm e}^2\rangle M_{\rm b}c^2}\right]\right\}. \tag{A.15}$$

where the upper sign refer to $\rm e^-$ and the lower sign to $\rm e^+$. The energy moments are computing in terms of the Fermi integrals and also in this case for $\rm e^-$ the non vanishing lower integration limit is included as a shift in the chemical potential,

$$\langle\epsilon_{\rm e^-}^n\rangle = (k_{\rm B}T)^n\,\frac{F_{n+2}((\mu_{\rm e}-\Delta)/(k_{\rm B}T))}{F_2((\mu_{\rm e}-\Delta)/(k_{\rm B}T))}, \tag{A.16}$$

$$\langle\epsilon_{\rm e^+}^n\rangle = (k_{\rm B}T)^n\,\frac{F_{n+2}(-\mu_{\rm e}/(k_{\rm B}T))}{F_2(-\mu_{\rm e}/(k_{\rm B}T))}. \tag{A.17}$$

We notice that the expressions we have derived for $\langle\sigma_\nu\rangle$ are similar, but different from the expressions reported in Horowitz & Li (1999).

In Figure 6, we have presented curves of equal electron and positron capture rates in the matter density-temperature plane. In Figure A1, we plot for completeness the ratio between the two rates over the full plane.

Appendix B. Model for atmospheric drag

In the following, we construct a model for the atmospheric drag applicable to the ejecta considered in this work. Those are arranged in two expanding thin rings above and below the orbital plane. At the relevant distances from the remnant, Newtonian physics is sufficient. We assume that each fluid element of the ring would follow an unbound orbit without the drag force provided by the artificial atmosphere. To compute the latter, we assume that artificial atmosphere swept up by the expanding ring becomes part of it, while the linear and angular momentum of infinitesimal ring sections remains unchanged by this merging. We regard this as a reasonable approximation for the behavior of the finite volume numerical scheme unless the ring density becomes comparable to the atmosphere density. Given the atmosphere density ρ_a and an effective projected area A_r of the ring, the increase in the mass m of the ring is $\dot{m} = A_r\rho_a v_s$, where v_s is the velocity of the ring surface. We further approximate $v_s \approx \dot{r}$, where $r^2 = R_r^2 + z_r^2$, where R_r and z_r are the ring radius and the z-offset of the ring. To get the projected area, we take the increase in thickness during the expansion into account by making the assumption $A_r \approx 4\pi a r^2$, where a is a constant denoting the effective fraction of the solid angle covered by ejecta. This holds exactly if the expansion can be described as uniform scaling.

Combining all the above assumptions, we obtain $\dot{m} = 4\pi a r^2\rho_a\dot{r}$. Using momentum and angular momentum conservation and a central gravitating mass M, a short

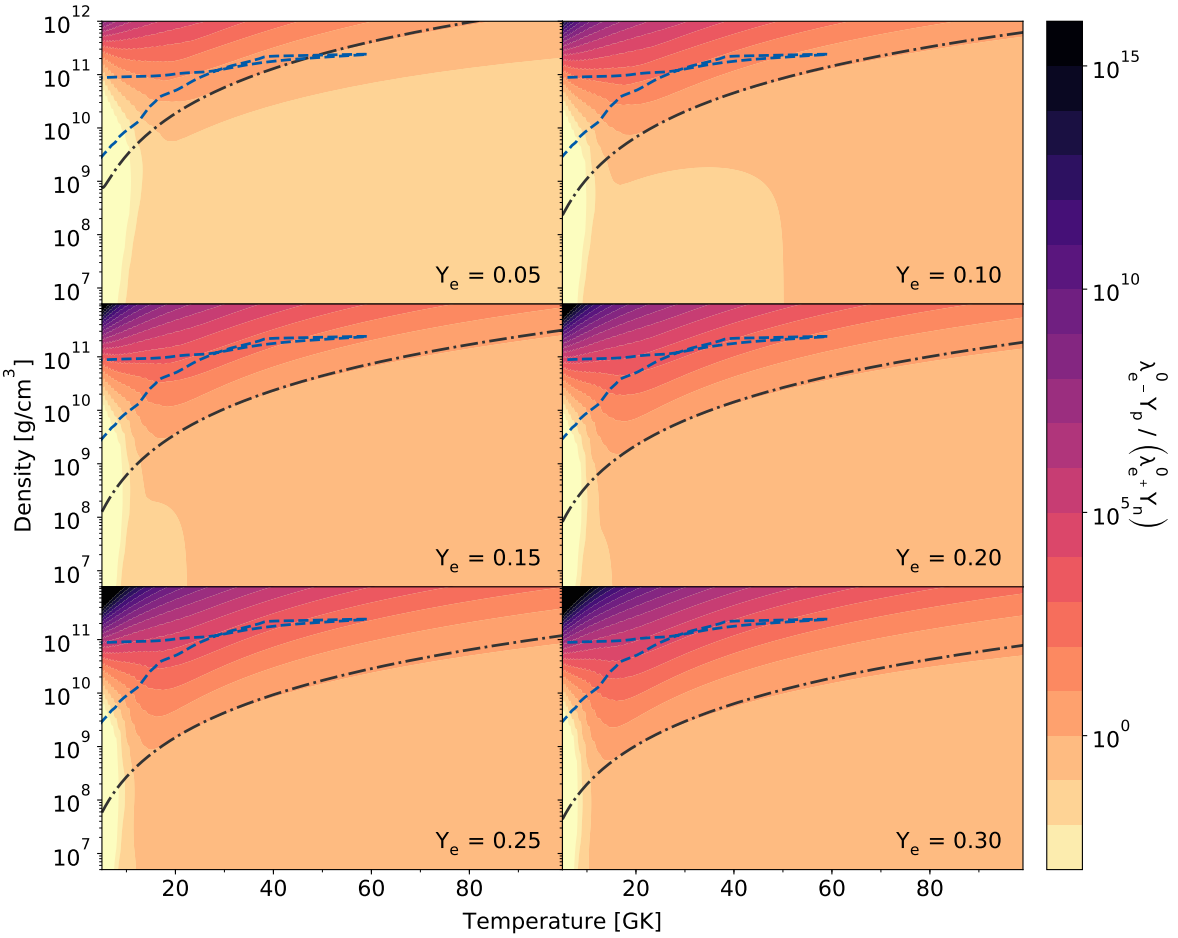

Figure A1. Ratio of the electron and positron capture rates in the density-temperature plane for varying electron fractions. We plot the trajectory from Figure 6 with a dashed blue line. The dotted-dashed black line marks the solution of Eqs. (26) for a composition made up of only nucleons.

computation yields

$$\frac{\mathrm{d}}{\mathrm{d}t}\left(\frac{E}{m}\right) = \frac{\mathrm{d}}{\mathrm{d}t}\left(\frac{E_k}{m} - \frac{M}{r}\right) = -2\frac{\dot{m}}{m}\frac{E_k}{m}, \qquad l^z = l_0^z\frac{m_0}{m}\,, \tag{B.1}$$

where E_k is the kinetic energy of the ring and l_z the specific angular momentum. Rewriting $m(t)$ as $m(r)$, we find

$$\frac{\mathrm{d}m}{\mathrm{d}r} = 4\pi a r^2 \rho_a, \qquad \frac{\mathrm{d}}{\mathrm{d}r}\left(mE\right) = -8\pi a \rho_a M m r\,, \tag{B.2}$$

Integration yields the result

$$m = m_0\left(1 + \frac{k_1}{3}\left(r^3 - r_0^3\right)\right) \tag{B.3}$$

$$\frac{E}{m} = \frac{m_0^2}{m^2}\left[\frac{E_0}{m_0} + Mk_1\left(\left(\frac{1}{3}k_1 r_0^3 - 1\right)\left(r^2 - r_0^2\right) - \frac{2}{15}k_1\left(r^5 - r_0^5\right)\right)\right], \tag{B.4}$$

where the subscripts $_0$ denote initial values and $k_1 = 4\pi a\rho_a/m_0$. A fit of k_1 to the extracted trajectories is shown in the middle panel of Figure B1 (we picked a starting

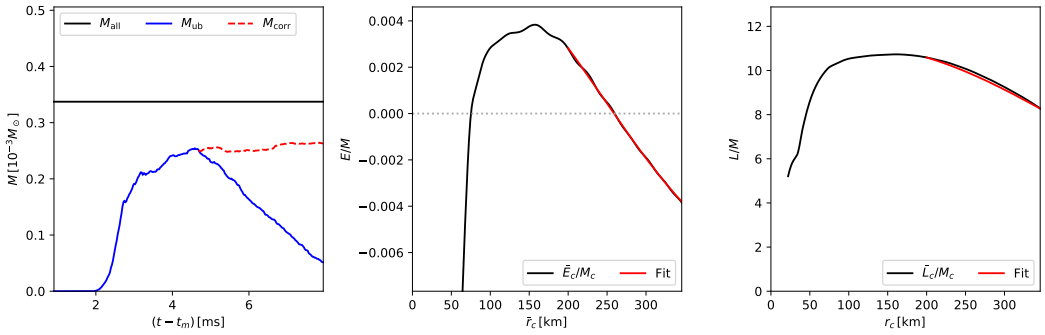

Figure B1. Influence of artificial atmosphere on ejecta. Left: total mass of tracers (black), tracer mass unbound at a given time according to geodesic criterion (blue), after correcting for the energy loss according to drag model fit (red). Middle: kinetic plus potential energy of tracers divided by total tracer mass (black), and the drag model fit (red). Right: total angular momentum of tracers divided by total tracer mass (black), and the drag model fit (red).

time well after the ring became unbound). Next, we computed the angular momentum using the fit parameter obtained above. The result is shown in the right panel, and fits the data sufficiently well. Our main requirement for the fit is however that it can account for the loss of unbound matter. To test this, we assume that the loss of (kinetic plus potential) specific energy for each ejecta fluid element is a function of radius given by the fit. We can then adjust the energy threshold for the geodesic bound matter criterion to correct for this energy loss. The result is shown in the left panel. After the correction, the sharp decrease is removed. Instead, we find a slight increase, which is likely an over-correction due to the various approximations. To avoid confusion, we note that the mass shown in the panel is not m in the equations above, but a sum over the (constant) tracer masses of the tracers which are unbound at a given time, i.e. it should remain constant if no tracer becomes bound/unbound anymore. In conclusion, our model supports the assumption that the slow-down of our ejecta is indeed just a numerical artifact, as assumed in (Kastaun et al. 2017) to compute the ejecta mass. The model might also be useful to plan numerical simulations since it allows to predict the slowing of the ejecta for given (constant) atmosphere density.

References

Baiotti L & Rezzolla L 2017 *Reports on Progress in Physics* **80**(9), 096901.
Barnes J, Kasen D, Wu M R & Martínez-Pinedo G 2016 *Astrophys. J.* **829**, 110.
Bauswein A, Ardevol Pulpillo R, Janka H T & Goriely S 2014 *ApJL* **795**, L9.
Bauswein A, Goriely S & Janka H T 2013 *ApJ* **773**, 78.
Bernuzzi S, Radice D, Ott C D, Roberts L F, Mösta P & Galeazzi F 2016 *PhRD* **94**(2), 024023.
Bludman S A & van Riper K A 1977 *ApJ* **212**, 859–872.
Bovard L, Martin D, Guercilena F, Arcones A, Rezzolla L & Korobkin O 2017 *ArXiv e-prints* .
Bovard L & Rezzolla L 2017 *ArXiv e-prints* .
Bruenn S W 1985 *ApJS* **58**, 771–841.

Cyburt R H, Amthor A M, Ferguson R, Meisel Z, Smith K, Warren S, Heger A, Hoffman R D, Rauscher T, Sakharuk A, Schatz H, Thielemann F K & Wiescher M 2010 *ApJS* **189**, 240–252.

Dessart L, Ott C D, Burrows A, Rosswog S & Livne E 2009 *ApJ* **690**, 1681–1705.

Eichler D, Livio M, Piran T & Schramm D N 1989 *Nature* **340**, 126–128.

Endrizzi A, Ciolfi R, Giacomazzo B, Kastaun W & Kawamura T 2016 *Classical and Quantum Gravity* **33**(16), 164001.
URL: *http://stacks.iop.org/0264-9381/33/i=16/a=164001*

Fernández R & Metzger B D 2016 *Annual Review of Nuclear and Particle Science* **66**, 23–45.

Foucart F, O'Connor E, Roberts L, Duez M D, Haas R, Kidder L E, Ott C D, Pfeiffer H P, Scheel M A & Szilagyi B 2015 *PhRD* **91**(12), 124021.

Freiburghaus C, Rosswog S & Thielemann F K 1999 *ApJL* **525**, L121–L124.

Fuller G M, Fowler W A & Newman M J 1982*a* *ApJ* **252**, 715–740.

Fuller G M, Fowler W A & Newman M J 1982*b* *ApJS* **48**, 279–319.

Fuller G M, Fowler W A & Newman M J 1985 *ApJ* **293**, 1–16.

Galeazzi F, Kastaun W, Rezzolla L & Font J A 2013 *PhRD* **88**(6), 064009.

Goriely S, Bauswein A, Just O, Pllumbi E & Janka H T 2015 *MNRAS* **452**, 3894–3904.

Hansen C J, Montes F & Arcones A 2014 *ApJ* **797**, 123.

Hempel M, Fischer T, Schaffner-Bielich J & Liebendörfer M 2012 *ApJ* **748**, 70.

Hoffman R D, Woosley S E & Qian Y Z 1997 *ApJ* **482**, 951–962.

Horowitz C J 2002 *PhRD* **65**(4), 043001.

Horowitz C J & Li G 1999 *PRL* **82**, 5198–5201.

Hotokezaka K, Kyutoku K, Okawa H, Shibata M & Kiuchi K 2011 *PhRD* **83**(12), 124008.

Käppeli R, Whitehouse S C, Scheidegger S, Pen U L & Liebendörfer M 2011 *ApJS* **195**, 20.

Kastaun W, Ciolfi R, Endrizzi A & Giacomazzo B 2017 *Phys. Rev. D* **96**, 043019.
URL: *https://link.aps.org/doi/10.1103/PhysRevD.96.043019*

Kastaun W & Galeazzi F 2015*a* *Phys. Rev. D* **91**, 064027.
URL: *http://link.aps.org/doi/10.1103/PhysRevD.91.064027*

Kastaun W & Galeazzi F 2015*b* *PhRD* **91**(6), 064027.

Korobkin O, Rosswog S, Arcones A & Winteler C 2012 *MNRAS* **426**, 1940–1949.

Kulkarni S R 2005 *ArXiv Astrophysics e-prints* .

Langanke K & Martínez-Pinedo G 2001 *At. Data Nucl. Data Tables* **79**, 1–46.

Lattimer J M, Mackie F, Ravenhall D G & Schramm D N 1977 *ApJ* **213**, 225–233.

Lodders K 2003 *ApJ* **591**, 1220–1247.

Martin D, Perego A, Arcones A, Thielemann F K, Korobkin O & Rosswog S 2015 *ApJ* **813**, 2.

Metzger B D, Martínez-Pinedo G, Darbha S, Quataert E, Arcones A, Kasen D, Thomas R, Nugent P, Panov I V & Zinner N T 2010 *MNRAS* **406**, 2650–2662.

Möller P, Nix J R, Myers W D & Swiatecki W J 1995 *At. Data Nucl. Data Tables* **59**(2), 185 – 381.
URL: *http://www.sciencedirect.com/science/article/pii/S0092640X85710029*

Möller P, Pfeiffer B & Kratz K L 2003 *PhRC* **67**(5), 055802.

Neilsen D, Liebling S L, Anderson M, Lehner L, O'Connor E & Palenzuela C 2014 *PhRD* **89**(10), 104029.

Panov I V, Kolbe E, Pfeiffer B, Rauscher T, Kratz K L & Thielemann F K 2005 *Nucl Phys A* **747**, 633–654.

Panov I V, Korneev I Y, Rauscher T, Martínez-Pinedo G, Kelić-Heil A, Zinner N T & Thielemann F K 2010 *A&A* **513**, A61.

Perego A, Cabezón R M & Käppeli R 2016 *ApJS* **223**, 22.

Perego A, Rosswog S, Cabezón R M, Korobkin O, Käppeli R, Arcones A & Liebendörfer M 2014 *MNRAS* **443**, 3134–3156.

Radice D, Bernuzzi S, Del Pozzo W, Roberts L F & Ott C D 2017 *ApJL* **842**, L10.

Radice D, Galeazzi F, Lippuner J, Roberts L F, Ott C D & Rezzolla L 2016 *MNRAS* **460**, 3255–3271.

Rauscher T 2003 *ApJS* **147**, 403–408.

Rauscher T & Thielemann F K 2000 *At. Data Nucl. Data Tables* **75**, 1–351.

Read J S, Baiotti L, Creighton J D E, Friedman J L, Giacomazzo B, Kyutoku K, Markakis C, Rezzolla L, Shibata M & Taniguchi K 2013 *PhRD* **88**(4), 044042.

Rezzolla L & Takami K 2016 *PhRD* **93**(12), 124051.

Roberts L F, Lippuner J, Duez M D, Faber J A, Foucart F, Lombardi, Jr. J C, Ning S, Ott C D & Ponce M 2017 *MNRAS* **464**, 3907–3919.

Rosswog S 2015 *Int. J. Mod. Phys. A* **24**, 30012.

Rosswog S & Liebendörfer M 2003 *MNRAS* **342**, 673–689.

Ruffert M, Janka H T, Takahashi K & Schaefer G 1997 *A&A* **319**, 122–153.

Sekiguchi Y, Kiuchi K, Kyutoku K & Shibata M 2015 *PhRD* **91**(6), 064059.

Sekiguchi Y, Kiuchi K, Kyutoku K, Shibata M & Taniguchi K 2016 *PhRD* **93**(12), 124046.

Shen G, Horowitz C J & Teige S 2010 *PhRC* **82**, 015806.
URL: *http://link.aps.org/doi/10.1103/PhysRevC.82.015806*

Shen G, Horowitz C J & Teige S 2011 *PhRC* **83**, 035802.
URL: *http://link.aps.org/doi/10.1103/PhysRevC.83.035802*

Siegel D M, Ciolfi R & Rezzolla L 2014 *ApJL* **785**, L6.

Takahashi K, El Eid M F & Hillebrandt W 1978 *A&A* **67**, 185–197.

Timmes F X & Swesty F D 2000 *ApJS* **126**, 501–516.

Wanajo S, Sekiguchi Y, Nishimura N, Kiuchi K, Kyutoku K & Shibata M 2014 *ApJL* **789**, L39.

Winteler C, Käppeli R, Perego A, Arcones A, Vasset N, Nishimura N, Liebendörfer M & Thielemann F K 2012 *ApJL* **750**, L22.